# *Structure of the planetary boundary layer over southeast England: modeling and measurements*

JOURNAL OF GEOPHYSICAL RESEARCH: ATMOSPHERES, VOL. 118, 7799–7818, doi:10.1002/jgrd.50621, 2013

# Structure of the planetary boundary layer over Southeast England: Modeling and measurements

Bo Xie,[1] J. C. R. Hunt,[2] D. J. Carruthers,[3] J. C. H. Fung,[1,4] and J. F. Barlow[5]

Received 22 May 2013; revised 28 June 2013; accepted 29 June 2013; published 30 July 2013.

[1] The Weather Research and Forecasting model was applied to analyze variations in the planetary boundary layer (PBL) structure over Southeast England including central and suburban London. The parameterizations and predictive skills of two nonlocal mixing PBL schemes, YSU and ACM2, and two local mixing PBL schemes, MYJ and MYNN2, were evaluated over a variety of stability conditions, with model predictions at a 3 km grid spacing. The PBL height predictions, which are critical for scaling turbulence and diffusion in meteorological and air quality models, show significant intra-scheme variance ($> 20\%$), and the reasons are presented. ACM2 diagnoses the PBL height thermodynamically using the bulk Richardson number method, which leads to a good agreement with the lidar data for both unstable and stable conditions. The modeled vertical profiles in the PBL, such as wind speed, turbulent kinetic energy (TKE), and heat flux, exhibit large spreads across the PBL schemes. The TKE predicted by MYJ were found to be too small and show much less diurnal variation as compared with observations over London. MYNN2 produces better TKE predictions at low levels than MYJ, but its turbulent length scale increases with height in the upper part of the strongly convective PBL, where it should decrease. The local PBL schemes considerably underestimate the entrainment heat fluxes for convective cases. The nonlocal PBL schemes exhibit stronger mixing in the mean wind fields under convective conditions than the local PBL schemes and agree better with large-eddy simulation (LES) studies.

**Citation:** Xie, B., J. C. R. Hunt, D. J. Carruthers, J. C. H. Fung, and J. F. Barlow (2013), Structure of the planetary boundary layer over Southeast England: Modeling and measurements, *J. Geophys. Res. Atmos.*, *118*, 7799–7818, doi:10.1002/jgrd.50621.

## 1. Introduction

### 1.1. Nonlocal and Local Mixing PBL Schemes

[2] Turbulent mixing of heat, momentum, moisture, and air pollutants has a strong influence over both meteorology and air quality in the planetary boundary layer (PBL) [*Nieuwstadt and Hunt*, 2003; *Baklanov et al.*, 2007]. The Weather Research and Forecasting (WRF) model has shown skills in predictive modeling of the main statistical atmospheric quantities. A number of local closure mixing PBL schemes (e.g., turbulent kinetic energy (TKE) closure schemes – the Mellor-Yamada-Janjić (MYJ) PBL scheme [*Janjić*, 1990, 2002] and the Mellor-Yamada-Nakanishi-Niino level 2.5 (MYNN2) PBL scheme [*Nakanishi and Niino*, 2009]) and nonlocal closure mixing PBL schemes (e.g., the Yonsei University (YSU) PBL scheme [*Hong et al.*, 2006; *Hong*, 2010] and the Asymmetric Convective Model version 2 (ACM2) PBL scheme [*Pleim*, 2007a, 2007b]) have been developed to simulate the turbulent PBL processes. The local closure PBL schemes are suited for shear turbulence in weakly stable conditions [*Mellor and Yamada*, 1982]. However, in the upper part of the convective PBL, the heat flux which is determined by large eddies is often counter to the local gradient, i.e., the flux can remain upward where the local potential temperature gradients are typically zero or positive. The upward heat flux arises from the nonlocal transport by buoyant plumes that initiate near the surface. Hence, large eddies on the scale of the convective PBL also produce turbulent mixing [*Hunt et al.*, 1988a]. Nonlocal closure PBL schemes are thus critical to the realistic production of eddy structure in a convective PBL. One kind of nonlocal schemes uses a countergradient adjustment term to represent the nonlocal upward transport by buoyant plumes [*Troen and Mahrt*, 1986; *Holtslag and Boville*, 1993; *Hong and Pan*, 1996], such as in the YSU PBL scheme. The other kind of nonlocal schemes represents the nonlocal mixing by the explicit treatment of the upward

[1]School of Science, Hong Kong University of Science and Technology, Kowloon, Hong Kong.
[2]Departments of Space and Climate Physics and Earth Sciences, University College London, London, UK.
[3]Cambridge Environment Research Consultants, Cambridge, UK.
[4]Department of Mathematics, Hong Kong University of Science and Technology, Kowloon, Hong Kong.
[5]Department of Meteorology, University of Reading, Reading, UK.

Corresponding author: J. C. H. Fung, Department of Mathematics, Hong Kong University of Science and Technology, Clear Water Bay, Kowloon, Hong Kong. (majfung@ust.hk)


2169-897X/13/10.1002/jgrd.50621

and downward transport of conserved atmospheric scalars [*Stull*, 1984; *Pleim and Chang*, 1992], such as in the ACM2 PBL scheme.

### 1.2. Objectives

[3] Although a number of studies [e.g., *Shin and Hong*, 2011; *García-Díez et al*., 2013] have been made to compare the predictions of the PBL by various physics schemes in the WRF model, many of them focus either on a case study of a particular PBL, which can be stability dependent, or on a statistical study by lumping different sky conditions over a long period, which can be affected by the cloud simulations. In addition, most of the studies have only compared the predictions with surface measurements of 2 m temperature and 10 m wind speed, because of the difficulty of obtaining measurements of the vertical mean quantities and high-order moments such as TKE and turbulent fluxes. Moreover, few studies have elucidated the model processes or related the modeled differences to the different parameterizations in each PBL scheme and its tied surface layer scheme. The PBL height is often defined as the mixed layer height plus part of the capping inversion depth in a convective PBL [*Hong et al*., 2006; *Pleim*, 2007a; *Wyngaard and Brost*, 1984]. The predictions of the PBL height are important for estimating the mean quantities such as the temperature and wind in meteorological models and are also critical for modeling the air pollutant dispersion [*Carruthers et al*., 1994; *Cimorelli et al*., 2005]. In this study, we consider the physical characteristics that define the PBL height in order to discuss the scheme-specific diagnostic methods. Recently, WRF version 3.4.1 corrected a bug in the numerical codes of the YSU PBL scheme for the stable PBL, which was predicted erroneously as always being neutral. ACM2 also has some updates in the eddy diffusivity in the new codes. As a relatively new TKE PBL scheme in WRF, MYNN2 was developed by considering effects of buoyancy on pressure covariances and effects of stability on the turbulent length scale, with a large-eddy simulation (LES) database. *Nakanishi and Niino* [2009] showed that MYNN2 improved the TKE predictions over the Mellor-Yamada model. All these PBL schemes require a rigorous evaluation of their predictions of different types of the PBL.

[4] An important indicator of the stability of the PBL is the dimensionless length scale $h/L$, defined as

$$\frac{h}{L} = \frac{-\kappa g \overline{(w'\theta_v')}_0 h}{\theta_{v0} u_*^3} \tag{1}$$

where $h$ is the PBL height, $L$ the Monin-Obukhov length, $\kappa$ the von Kármán constant (0.4), $g$ the gravitational acceleration, $\overline{(w'\theta_v')}_0$ the surface kinematic heat flux, $\theta_{v0}$ the virtual potential temperature near the surface, and $u_*$ the friction velocity. The range of stability conditions in a mid-high latitude region dominated by maritime air masses, e.g., the United Kingdom (UK), can be quite different from that in a tropical or subtropical region (e.g., Hong Kong). With reference to the modeling study of *Xie et al*. [2012], the surface heating is usually strong in the tropics; thus, even in a winter month, such as November, the simulated daytime peak value of $-h/L$ can be larger than 20, whereas in the UK, it is typically smaller than 5. Furthermore, after sunset, the winds persist in the UK, so that the nocturnal PBL is typically less stable than that in the subtropics. Thus, computations here are focused on the PBL structures in a region that is characteristic of relatively weak heating and strong wind shear [cf. *Holtslag and Boville*, 1993; *Xie et al*., 2012]. In addition to comparing the simulation results with the standard meteorological measurements of 2 m temperature and 10 m wind across Southeast (SE) England, comparisons are also made with new field measurements [*Harrison et al*., 2012] and new simulation results [*Bohnenstengel et al*., 2011] over London using the UK Met Office Unified Model. We evaluate the parameterizations of nonlocal and local mixing PBL schemes in the WRF model for a range of stability conditions. The modeled controlling variables of surface sensible heat flux, PBL height $h$, convective velocity scale $w_*$, friction velocity $u_*$, $h/L$ and also the vertical profiles of potential temperature, wind speed, eddy diffusivity, turbulent length scale, TKE, and heat flux are presented. Since the modeled vertical profiles of mean and turbulent quantities vary greatly with different PBL schemes [*Xie et al*., 2012], a detailed assessment is needed for improving numerical weather prediction and air quality modeling [e.g., *Kwok et al*., 2012; *Zhang et al*., 2012]. This study discusses the physical rationale of the profile differences, compares the eddy structures and entrainment heat fluxes with previous LES results, and validates the PBL height and TKE predictions with a valuable data set over London.

[5] Section 2 briefly describes the meteorological sites, instruments, and data selection. Section 3 provides descriptions of the model setup and configurations including the study's domain definition and key physics options. Section 4 presents the surface and vertical meteorological predictions with different PBL schemes and their comparisons with observations across SE England. Concluding remarks follow in the final section of the study.

## 2. Meteorological Sites, Instruments, and Data Selection

[6] The temperature measured at 2 m above ground level (AGL) and the wind measured at 10 m AGL were collected at eight meteorological sites across SE England for both June and November 2007. Figure 1a depicts the distribution of these sites. The red dots indicate urban grid sites and the blue dots indicate rural grid sites. The PBL height determined from the Doppler lidar observations of the vertical velocity variance, and TKE measured by the sonics in central London were taken during the REPARTEE 2007 campaign. An overview of the campaign and the instruments such as the Doppler lidar and sonics was described by *Harrison et al*. [2012]. The rooftop and the British Telecom (BT) Tower details were given in a study by *Barlow et al*. [2009]. The rooftop conditions were monitored on the Westminster City Council (WCC) building using sonics at a height of 2 m above the rooftop, i.e., 17 m AGL. An additional sonic was installed on the top of the BT Tower at a measurement height of 190 m AGL. This is the tallest building within several kilometers of the site, with good exposure to winds in all directions. As shown in Figure 1b, the BT Tower is approximately 1.6 km to the east of the WCC building and 1.2 km to the east of the lidar site. The TKE observations at the rooftop are available for the first half of November, and the TKE observations at the BT tower are available throughout

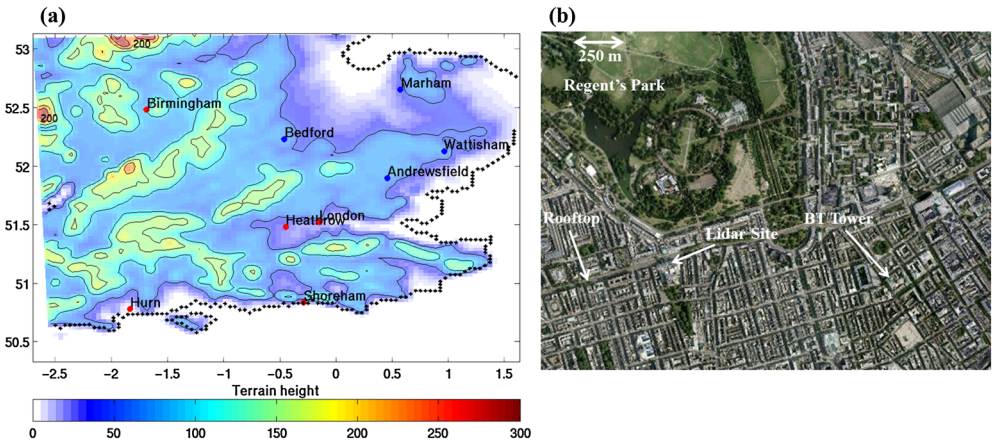


**Figure 1.** (a) Meteorological sites distribution across SE England (red dots: urban grids; blue dots: rural grids) and (b) site and instrument locations in central London.

November, although they are patchy (about 30% availability) before mid-November.

[7] In line with *Barlow et al*. [2011], the vertical velocity variance ($\overline{w'^2}$) data measured by the lidar were used to determine the PBL height. The variance gives a measure of the vertical turbulence intensity. Vertical profiles of the variance from the ground up were examined. The height at which the variance dropped below the threshold ($\overline{w'^2} < 0.1\ \mathrm{m^2/s^2}$) was assumed to be the top of the PBL. The analyses and possible errors of the measurements were given by *Barlow et al*. [2009, 2011] and *Harrison et al*. [2012].

## 3. Model Setup, Configurations, and Physics Options

### 3.1. Domain Settings

[8] Three nested domains with horizontal grid spacings of 27 km, 9 km, and 3 km, respectively, were used. Figure 2 shows the geographic coverage of the three domains. Specifically, Domain 1 (120 × 120) covers much of Europe and the Northeast Atlantic Ocean, Domain 2 (129 × 144) covers the UK, and Domain 3 (96 × 102) covers SE England centering on Greater London. A Lambert conformal map projection was used with the projection parameters set as follows: $\alpha = 40°$, $\beta = 60°$, $\gamma = -0.1°$, center longitude = 0.1°W, and center latitude = 51.5°N.

[9] The terrain-following coordinate in the WRF model setup contains 50 full sigma levels. The model's lowest five full sigma levels above the surface are 0.9979, 0.9956, 0.9931, 0.9904, and 0.9875. The corresponding heights are around 17.5, 37, 57, 80, and 104 m AGL, respectively. The layer thickness increases gradually with height. The model top pressure is set to 50 hPa, about 20 km AGL. Twenty-one sigma levels were assigned to occupy the lowest 2 km AGL.

### 3.2. WRF Configurations

[10] The lateral boundary conditions for the outermost domain and the initial conditions for all of the domains were obtained from the National Centers for Environmental Prediction Final Operational Global Analysis data. The data has a horizontal resolution of 1° in latitude and longitude and a 6 h temporal resolution. WRF version 3.4.1 was used in this study. The Rapid Radiative Transfer Model longwave radiation scheme, the Dudhia shortwave radiation scheme, the WRF single-moment three-class microphysics scheme, and the Noah Land Surface Model were applied in all domains. The Grell-Devenyi ensemble cumulus scheme was applied in Domains 1 and 2. One-way nesting was applied between the domains [*Skamarock et al*., 2008]. The simulations were conducted for June and November 2007. Each consecutive simulation ran for 4 days, with the first day considered as spin-up.

### 3.3. PBL and Surface Layer Schemes

[11] Four PBL schemes are studied here, including two nonlocal mixing PBL schemes (YSU and ACM2) and two local mixing PBL schemes (MYJ and MYNN2). *Xie et al*. [2012] gave brief descriptions of the YSU, ACM2, and MYJ PBL schemes and the surface layer schemes. Here, we provide some key features of the MYNN2 PBL scheme. The governing equations of TKE in the MYNN2 PBL scheme are

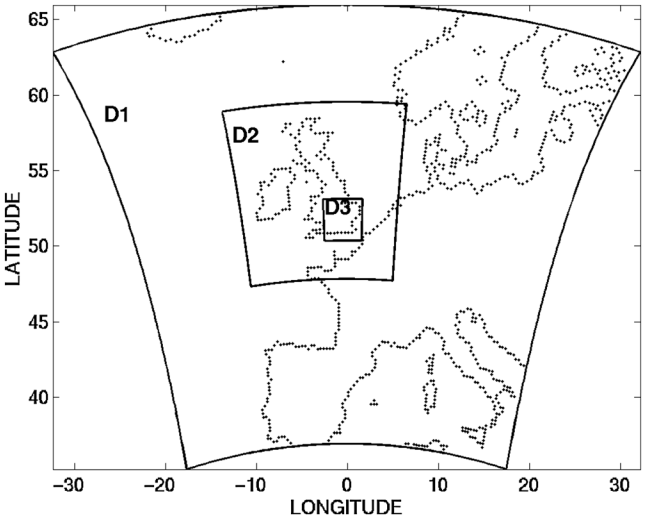


**Figure 2.** Horizontal coverage used for the three domains in the WRF simulations.

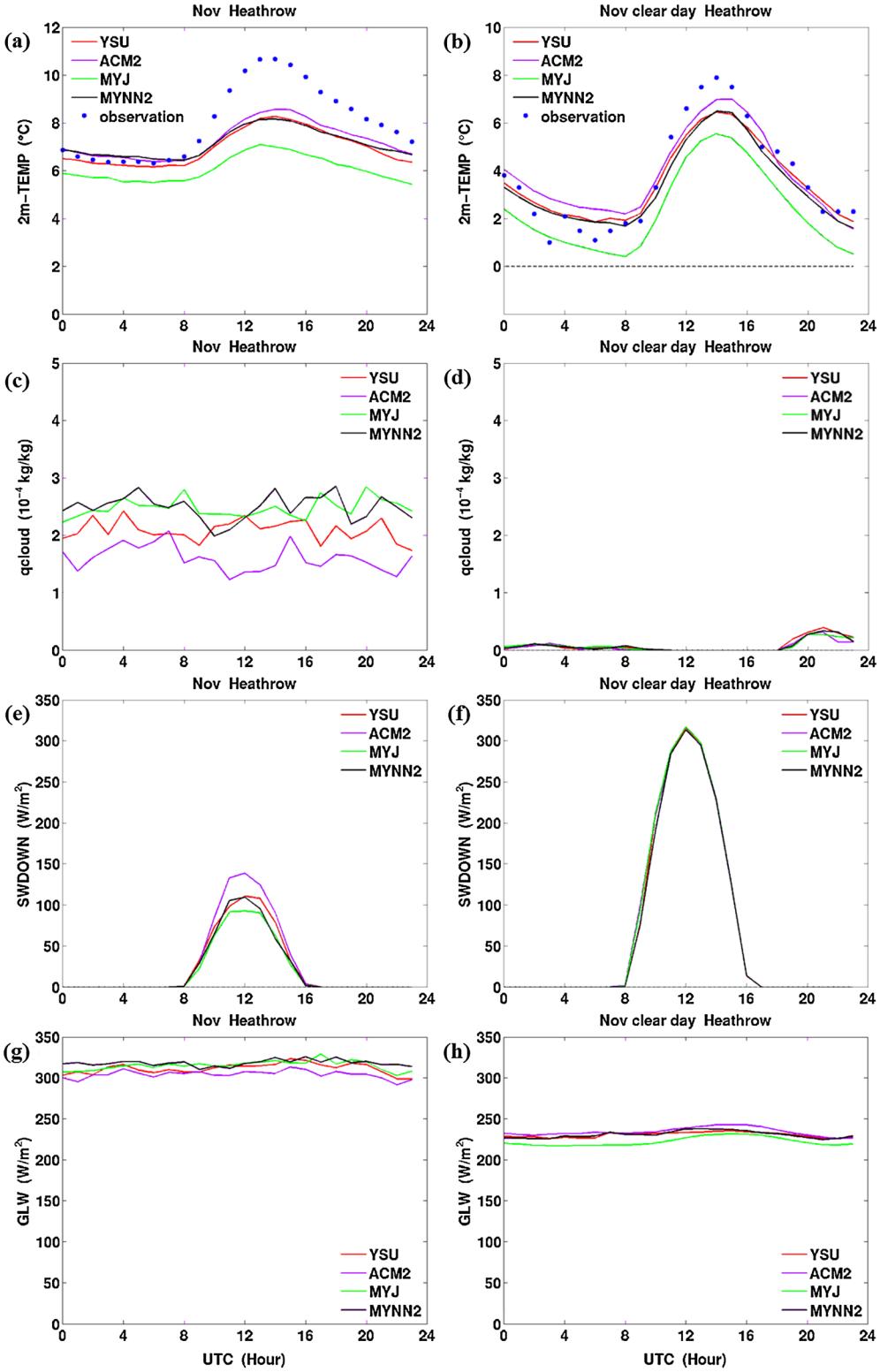


**Figure 3.** 2 m temperature averaged (a) over November and (b) on a clear day, 12 November; cloud water mixing ratio averaged (c) over November and (d) on 12 November; downward shortwave radiation at surface averaged (e) over November and (f) on 12 November; downward longwave radiation at surface averaged (g) over November and (h) on 12 November at Heathrow.

**Table 1.** Model Performance in 2 m Temperature for 3 km WRF Simulations Averaged at Eight Sites Across SE England Over the Period of June and November 2007

| | YSU | ACM2 | MYJ | MYNN2 |
|---|---|---|---|---|
| *2 m temperature (°C) in Jun* | | | | |
| Index of Agreement | 0.88 | **0.89** | 0.88 | 0.87 |
| RMSE | 2.10 | **1.99** | 2.14 | 2.14 |
| MB | −1.15 | **−0.99** | −1.16 | −1.18 |
| *2 m temperature (°C) in Nov* | | | | |
| Index of Agreement | 0.91 | **0.93** | 0.87 | 0.91 |
| RMSE | 1.96 | **1.80** | 2.45 | 1.98 |
| MB | −0.74 | **−0.57** | −1.52 | **−0.55** |

$$\frac{\partial q^2}{\partial t} = -\frac{\partial}{\partial z}\overline{w'\left(q^2 + 2\frac{p'}{\rho_0}\right)} - 2\left(\overline{u'w'}\frac{\partial \overline{u}}{\partial z} + \overline{v'w'}\frac{\partial \overline{v}}{\partial z}\right) + 2\frac{g}{\theta_0}\overline{w'\theta_v'} - 2\varepsilon \quad (2)$$

$$q^2 = \overline{u'^2} + \overline{v'^2} + \overline{w'^2} \quad (3)$$

$$-\overline{w'\left(q^2 + 2\frac{p'}{\rho_0}\right)} = K_q\frac{\partial q^2}{\partial z} \quad (4)$$

$$-\overline{w'c'} = K_c\frac{\partial \overline{c}}{\partial z} \quad (5)$$

$$K_c = l_E q S_c \quad (6)$$

where the small letters with prime denote turbulent variables, the overbar an ensemble average, and the subscript 0 a reference state. $q^2/2$ is the TKE per unit mass, $(u', v', w')$ the turbulent velocity components, $p$ the pressure, $\rho$ the air density, $\theta$ the potential temperature, $\theta_v$ the virtual potential temperature, and $\varepsilon$ the TKE dissipation rate. The second- and third-order turbulent fluxes in equations (4) and (5) are expressed in the form of down-gradient diffusion, where $c$ represents the quantity $u$, $v$, or $\theta$; $K_c$ the eddy diffusivity; $l_E$ the turbulent length scale; and $S_c$ the stability function. MYNN2 improves several weak points of the Mellor-Yamada model such as the underestimations of the TKE and the turbulent length scale, the neglect of buoyancy effects on the pressure covariances, and the stability functions for third-order turbulent fluxes [*Nakanishi and Niino*, 2009]. *Moeng and Wyngaard* [1986] showed the importance of the buoyancy correction on the pressure covariances (e.g., $\frac{1}{\rho_0}\overline{\theta'\frac{\partial p'}{\partial z}}$) in the scalar-flux equation.

[12] Note that there are limitations to the allowable combinations of the PBL and surface layer schemes. To reduce the impact introduced by different surface layer schemes, YSU, ACM2 and MYNN2 were run with the MM5-similarity surface layer scheme. MYJ, however, can only be run with the Eta-similarity surface layer scheme. The differences caused by these two surface layer schemes are also discussed in this study (section 4.2).

## 4. WRF Simulations Across SE England in June and November

[13] The WRF simulations at a 3 km grid spacing were compared with the surface measurements taken at eight sites across SE England. Of these sites, Heathrow, Birmingham, Hurn, and Shoreham are represented by urban grids, whereas Andrewsfield, Bedford, Marham, and Wattisham are represented by rural grids in the model, as shown in Figure 1a. The urban and rural grids in the model are distinguished by parameterizations of albedo, roughness, stomatal resistance, leaf area index, and green vegetation fraction. No buildings are modeled explicitly in this study. All of the times refer to UTC. The results at Heathrow and Andrewsfield are the focus of this study and assumed to be representative of urban and rural grids, respectively.

### 4.1. Monthly Mean 2 m Temperature and 10 m Wind

[14] In June, the differences in 2 m temperature and 10 m wind speed across the PBL schemes are small. Model runs for each of the PBL schemes broadly reproduce the diurnal variations of 2 m temperature and 10 m wind speed in comparison with the measurements. In November, all the runs underestimate the peak daytime 2 m temperature (Figure 3a). This may stem from an under-prediction of the simulated insolation, which is strongly dependent on the simulated cloud cover [*Xie et al*., 2012]. It is possible that all the simulations predict clouds that are too thick or produce too much attenuation on the insolation. The local PBL scheme MYJ considerably underestimates both the daytime and nighttime 2 m temperatures in November (Figure 3a). This is partly related to its tied Eta-similarity surface layer scheme, which is discussed in section 4.2. The diurnal variations in 10 m wind speed simulated by all the runs are also not as strong as the observations in November. The 10 m wind direction is well produced by all the runs in both June and November, although the run with ACM2 is slightly better than the others. Tables 1 and 2 summarize the statistics of the WRF performances for the different PBL schemes. The statistics were calculated using a time series of hourly 2 m temperatures and 10 m wind speeds for the entire month at each site and then averaged over the eight sites across SE England. The statistics shown are the index of agreement, root mean squared error (RMSE), and mean bias (MB). The index of agreement reflects the degree to which the observed variable is accurately estimated by the simulation [*Willmott*, 1981]. The boldface in the table indicates the best statistics among the different runs. Overall, ACM2 performs best on most of the statistical measures.

[15] An additional microphysics scheme and a cumulus scheme were used to test their sensitivities to the temperature simulations in November. However, in comparison with the WRF single-moment three-class microphysics scheme used in this study, the WRF single-moment six-class microphysics

**Table 2.** Model Performance in 10 m Wind Speed for 3 km WRF Simulations Averaged at Eight Sites Across SE England Over the Period of June and November 2007

| | YSU | ACM2 | MYJ | MYNN2 |
|---|---|---|---|---|
| *10 m wind speed (m/s) in Jun* | | | | |
| Index of Agreement | 0.83 | **0.85** | 0.82 | 0.83 |
| RMSE | 1.46 | **1.42** | 1.50 | 1.46 |
| MB | −0.47 | **−0.26** | −0.50 | −0.43 |
| *10 m wind speed (m/s) in Nov* | | | | |
| Index of Agreement | 0.87 | **0.89** | 0.88 | 0.87 |
| RMSE | 1.45 | **1.30** | 1.36 | 1.37 |
| MB | 0.07 | 0.36 | 0.05 | **0.02** |

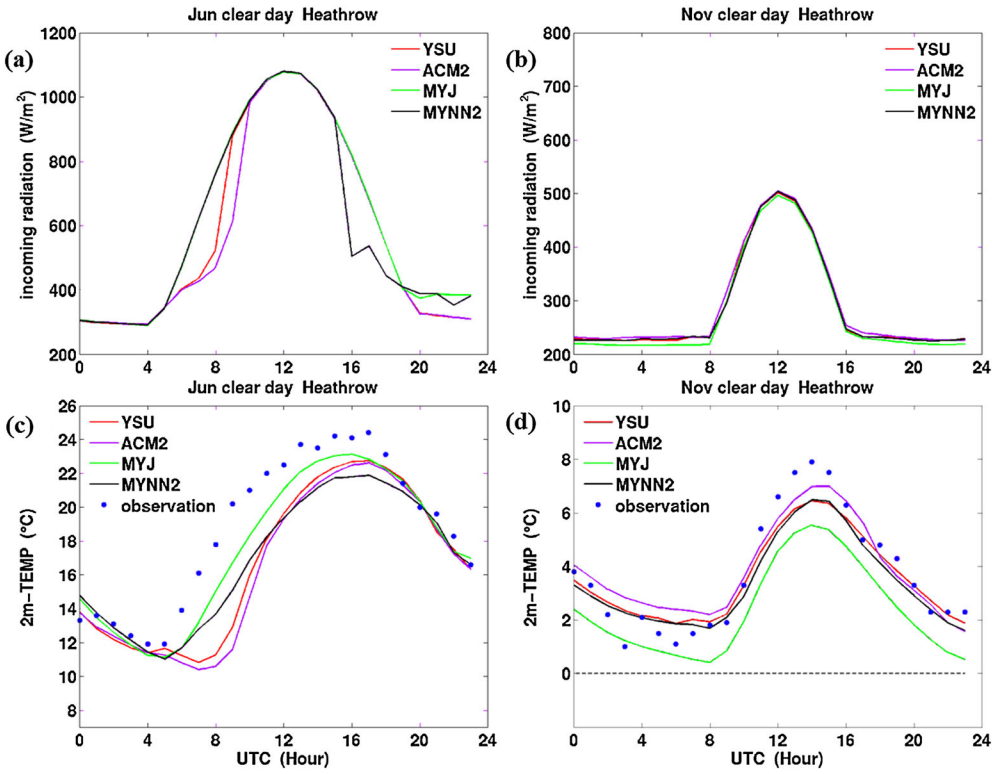


**Figure 4.** Incoming radiation on clear days of (a) 2 June and (b) 12 November; 2 m temperature on clear days of (c) 2 June and (d) 12 November at Heathrow.

scheme exhibits only a small impact on 2 m temperature simulations (< 0.5°C). Moreover, it does not strengthen the diurnal variations. A comparison with an additional model run using the Kain-Fritsch cumulus shows the temperature simulations to be insensitive to the choice of cumulus scheme for these simulation periods. To investigate the cloud impact, the average WRF simulation results over the entire month of November were compared with those over the clear days. A clear day was defined as when the cloud water mixing ratio predicted by all the runs and the observed cloud amount are marginal, e.g., 12 November at Heathrow (Figure 3d). The modeled downward shortwave radiation at surface (Figures 3e and 3f) is attenuated on cloudy days, whereas the modeled downward longwave radiation at surface (Figures 3g and 3h) is intensified. The simulations involving all the PBL schemes exhibit stronger diurnal variations in 2 m temperature on the clear day (Figure 3b) that fit well with observations. The PBL schemes, especially ACM2, give better predictions under a clear sky where the insolation is not much affected by cloud cover. Therefore, the cloud or its relation to insolation may not be well resolved across SE England in November. However, the cloud processes, which are coupled with microphysics, cumulus, radiation, land surface physics, and PBL schemes in the WRF model, are intricate and beyond the scope of this study. Therefore, in the following sections, we will focus mainly on the PBL structures modeled by different PBL schemes under clear skies.

### 4.2. 2 m Temperature Under a Clear Sky

[16] Model simulations are presented for 2 June and 12 November 2007 when all the runs involving different PBL schemes predict marginal cloud water mixing ratios and similar peak incoming radiations, including both shortwave and longwave radiations (Figures 4a and 4b). These 2 days exhibit strong diurnal variations in 2 m temperature (Figures 4c and 4d) and relatively low wind conditions; there were no precipitation recorded affecting the atmospheric conditions.

[17] Figure 5 depicts the simulated diurnal variations in the surface sensible heat flux, near-surface temperature gradient ($T_{sfc} - T_{2m}$), heat exchange coefficient ($C_h$), and surface skin temperature ($T_{sfc}$) at Heathrow under clear skies. The surface sensible heat flux $H_0$ is parameterized as

$$H_0 = \rho C_p C_h U(z_1)\left[\theta_{sfc} - \theta(z_1)\right] \propto C_h U(z_1)\left[T_{sfc} - T_{2m}\right] \qquad (7)$$

where $C_p$ is the specific heat capacity of air at a constant pressure, $U(z_1)$ the wind speed at the lowest model layer height $z_1$, and $T$ the temperature. The subscripts *sfc* and 2*m* denote the variables at the surface and at 2 m. The latent heat flux is parameterized similarly to be proportional to $C_h$ and the near-surface water vapor mixing ratio gradient. The modeled latent heat flux is often small over the urban grid but large over the rural grid. The MYJ run with the Eta-similarity surface layer scheme (MYJ-Eta) computes smaller near-surface temperature gradients (Figures 5c and 5d) and noticeably larger heat exchange coefficients $C_h$ (Figures 5e and 5f) in the daytime than the other runs with the MM5-similarity surface layer scheme. The larger $C_h$ in the MYJ-Eta run lead to larger surface sensible heat fluxes (Figures 5a and 5b) and larger latent heat fluxes (not shown) than the other runs, resulting in larger energy losses at surface, hence lower surface skin temperatures (Figures 5g and 5h) during the

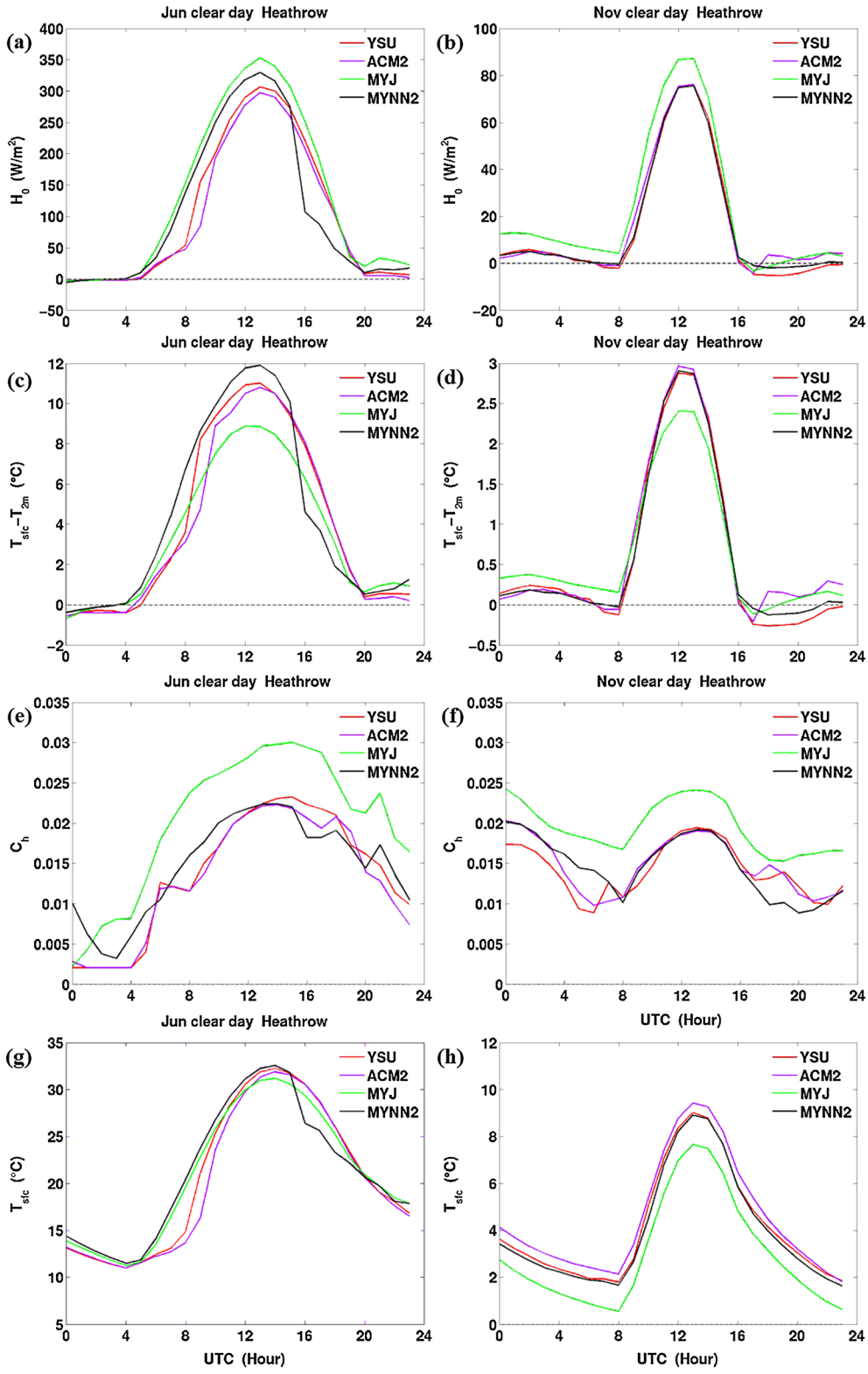


**Figure 5.** Surface sensible heat flux on (a) 2 June and (b) 12 November; near-surface temperature gradient on (c) 2 June and (d) 12 November; heat exchange coefficient on (e) 2 June and (f) 12 November; surface skin temperature on (g) 2 June and (h) 12 November at Heathrow.

daytime. This impact introduced by different $C_h$ was elucidated by *Xie et al*. [2012]. With the larger $C_h$, the MYJ-Eta run produces stronger mixing in the surface layer than the other runs with the MM5-similarity surface layer scheme. On the clear day in June, the MYJ-Eta run predicts larger daytime 2 m temperatures (Figure 4c) due to the stronger mixing, even when its predicted daytime surface skin temperatures are smaller than the other runs (Figure 5g). This is

similar to both the June and November cases in Hong Kong [*Xie et al*., 2012] in terms of the strong surface heat fluxes and large near-surface temperature gradients. However, on the clear day in November, due to the small near-surface temperature gradients within 3°C (Figure 5d), the lower surface skin temperatures in the MYJ-Eta run (Figure 5h) lead to lower 2 m temperatures (Figure 4d) despite the MYJ-Eta run predicting larger $C_h$. Therefore, the large underestimation of 2 m temperatures predicted by the MYJ-Eta run in November across SE England is partly attributable to the Eta-similarity surface layer scheme.

### 4.3. Boundary Layer Height

[18] The model predictions of the PBL height $h$ vary considerably, and this is a major cause of uncertainty of predictions of weather and air quality. In the meteorological context, the PBL height is important for scaling the turbulence within a PBL as used in the nonlocal PBL schemes YSU and ACM2. The eddy viscosity within a PBL in the nonlocal PBL schemes is parameterized as

$$K_m = \frac{\kappa u_* z}{\phi_m}\left(1-\frac{z}{h}\right)^2 \tag{8}$$

where the dimensionless stability function for momentum is formulated as $\phi_m = \left(1-16\frac{z_s}{L}\right)^{-1/4}$. ACM2 defines $z_s$ within the surface layer, i.e., $z_s = \min(z,\ 0.1h)$, whereas YSU defines it within the PBL. In the air quality context, air quality models usually use $h$ to compute the eddy diffusivity for heat and the eddy viscosity for momentum, depending on the vertical diffusion schemes. Therefore, even though $h$ is not used in the prognostic equations in the TKE PBL schemes (e.g., MYJ and MYNN2) for meteorological modeling, it is still important as input to the air quality models.

#### 4.3.1. Boundary Layer Height Formulations Over Land

##### 4.3.1.1. Formulations in YSU PBL Scheme

[19] The PBL height in YSU is diagnosed over land when the bulk Richardson number $Ri_b$ reaches a critical value $Ri_{bcr}$ as follows.

[20] In stable conditions,

$$Ri_b = \frac{gz[\theta_v(z)-\theta_v(z_1)]}{\theta_v(z_1)U(z)^2} \tag{9}$$

where $U(z)$ is the wind speed at a height $z$ and $Ri_{bcr}=0.25$. The PBL height is diagnosed as $h = Ri_{bcr}\frac{\theta_v(z_1)U(h)^2}{g[\theta_v(h)-\theta_v(z_1)]}$.

[21] In unstable conditions,

$$Ri_b = \frac{gz[\theta_v(z)-\theta_s]}{\theta_v(z_1)U(z)^2} \tag{10}$$

where $\theta_s = \theta_v(z_1)+\theta_T$ and $Ri_{bcr}=0$. $\theta_T$ is the virtual potential temperature excess [*Hong et al*., 2006], which is defined as

$$\theta_T = a\frac{\overline{(w'\theta_v')}_0}{w_{s0}} \tag{11}$$

where $a=6.8$ and $w_{s0}$ is the mixed layer velocity scale.

##### 4.3.1.2. Formulations in ACM2 PBL Scheme

[22] In stable conditions, ACM2 uses a similar formula to that in YSU but takes into account the bulk wind shear between a model layer and the lowest model layer,

$$Ri_b = \frac{g[\theta_v(z)-\theta(z_1)](z-z_1)}{\overline{\theta_v}\left([u(z)-u(z_1)]^2+[v(z)-v(z_1)]^2\right)} \tag{12}$$

where $\overline{\theta_v} = [\theta_v(z)+\theta(z_1)]/2$, $u$, and $v$ are the zonal and meridional wind components.

[23] In unstable conditions, ACM2 applies the bulk Richardson number method over the stably stratified entrainment layer only. First, the top of the convectively unstable layer ($z_{mix}$) is found as the height at which $\theta_v(z_{mix})=\theta_s$, where $\theta_s$ is defined similarly as YSU. The bulk Richardson number is then defined for the entrainment layer above $z_{mix}$ such that

$$Ri_b = \frac{g[\theta_v(z)-\theta_v(z_{mix})](z-z_{mix})}{\overline{\theta_v}\left([u(z)-u(z_{mix})]^2+[v(z)-v(z_{mix})]^2\right)} \tag{13}$$

[24] The PBL height is diagnosed when $Ri_b$ is equal to $Ri_{bcr}$, which is 0.25 for both unstable and stable conditions.

##### 4.3.1.3. Formulations in MYJ PBL Scheme

[25] The PBL height is defined as the height of the model layer where the TKE decreases to a minimum value of 0.1 $m^2/s^2$.

##### 4.3.1.4. Formulations in MYNN2 PBL Scheme

[26] A hybrid definition is implemented that uses both the theta-increase and TKE methods. The PBL height $h_\theta$ diagnosed by the theta-increase method is defined as

$$\theta_v(h_\theta) = \theta_{v\min} + 1.5 \tag{14}$$

where $\theta_{v\min}$ is the lowest virtual potential temperature within 500 m AGL. The PBL height $h_e$ diagnosed by the TKE method is defined as

$$\mathrm{TKE}(h_e) = \mathrm{TKE}_{cr} \tag{15}$$

where $\mathrm{TKE}_{cr}$ is the critical TKE value defined as the maximum TKE within 500 m AGL divided by 20, with an upper bound of 0.25 $m^2/s^2$ and a lower bound of 0.025 $m^2/s^2$. The PBL height is then diagnosed with a weighting function $w_f$,

$$w_f = 0.5\tanh\left(\frac{h_\theta-200}{400}\right)+0.5 \tag{16}$$

$$h = h_e(1-w_f)+h_\theta w_f \tag{17}$$

#### 4.3.2. Boundary Layer Height Formulation Limitations

[27] The vertical profiles of $\theta$ and TKE in the convective PBL at 2 P.M. on 3 November (Figures 6a and 6b) at Heathrow and on 16 November (Figures 6c and 6d) at Andrewsfield are depicted to show the differences in the diagnosed PBL heights across the PBL schemes, and the limitations of the PBL height diagnostic formulations in MYJ and MYNN2. Although the skies are cloudy on 3 and 16 November, the focus here is on probing the limitations of the PBL height diagnostic formulations. The horizontal dashed lines in Figure 6 represent the PBL heights diagnosed by each PBL scheme. The TKE (Figures 6b and 6d) are only predicted by the local TKE PBL schemes MYJ and MYNN2.

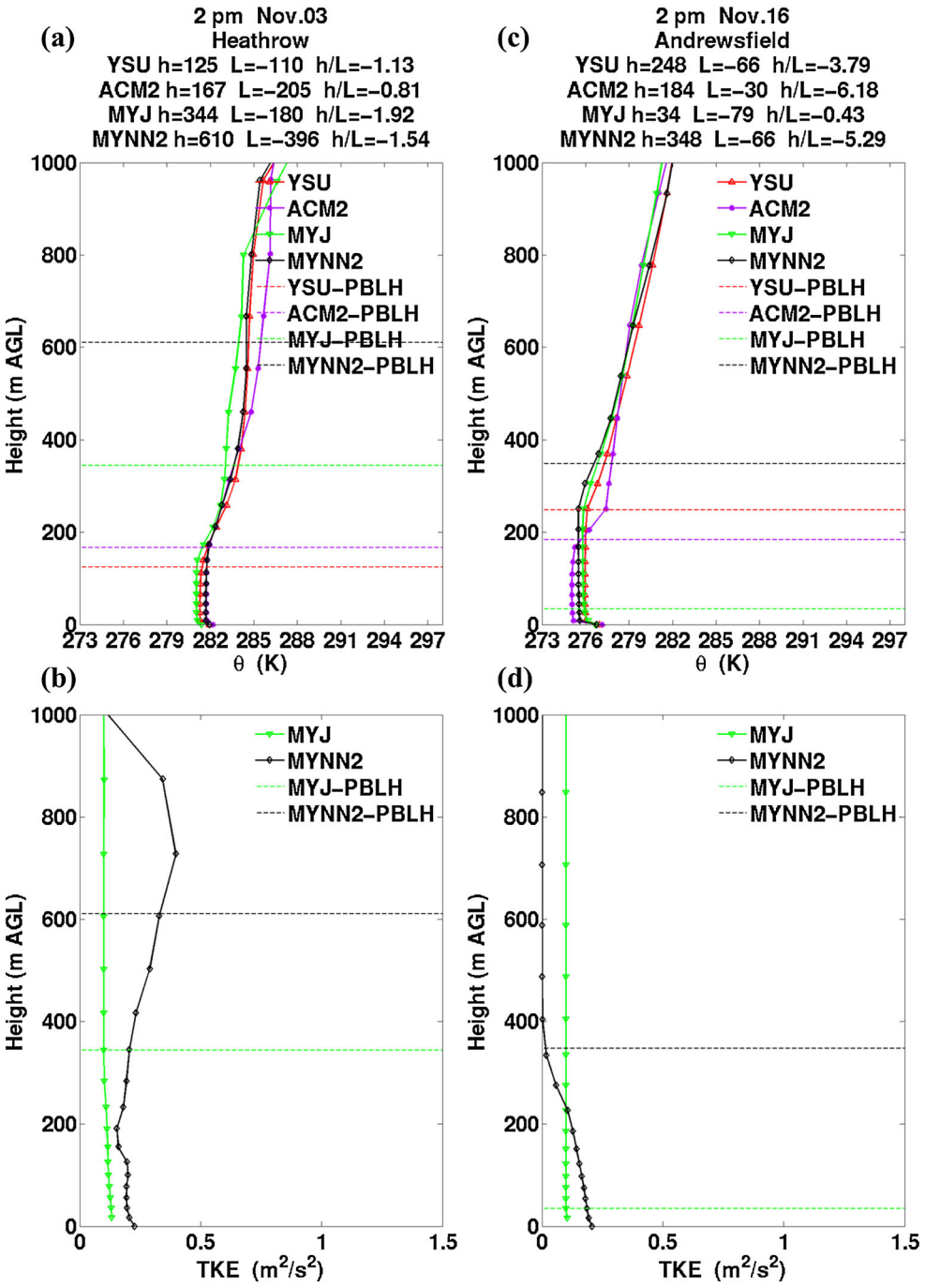


**Figure 6.** Vertical profiles at 2 P.M. on 3 November at Heathrow: (a) potential temperature and (b) TKE; vertical profiles at 2 P.M. on 16 November at Andrewsfield: (c) potential temperature and (d) TKE (horizontal dashed lines represent the PBL heights diagnosed by each PBL scheme).

[28] The minimum TKE method in MYJ can yield a PBL top that is much higher than the inversion base. On 3 November, all the runs with different PBL schemes estimate the inversion base heights at about 120–170 m AGL (Figure 6a). The interfacial layer between the inversion base and the PBL top is regarded as part of the entrainment layer. However, MYJ predicts a PBL top at 344 m AGL where the TKE decreases to 0.1 $m^2/s^2$ (Figure 6b) and an interfacial layer with a vertical extent of about 220 m, which is about twice the mixed layer depth. This seems unrealistic, as a convective PBL normally consists of a relatively shallow entrainment layer above a mixed layer. Therefore, the PBL height definition in MYJ is questionable, since above the PBL top, the TKE can be produced by processes such as wind shear and internal waves. On 16 November, the minimum TKE method in MYJ produces a significantly lower $h$ (34 m AGL) than the other PBL schemes because the predicted TKE is uniformly at the minimum value of 0.1 $m^2/s^2$ (Figure 6d). This implies that the TKE prognostic equations in MYJ require modifications, since the wind shear near the

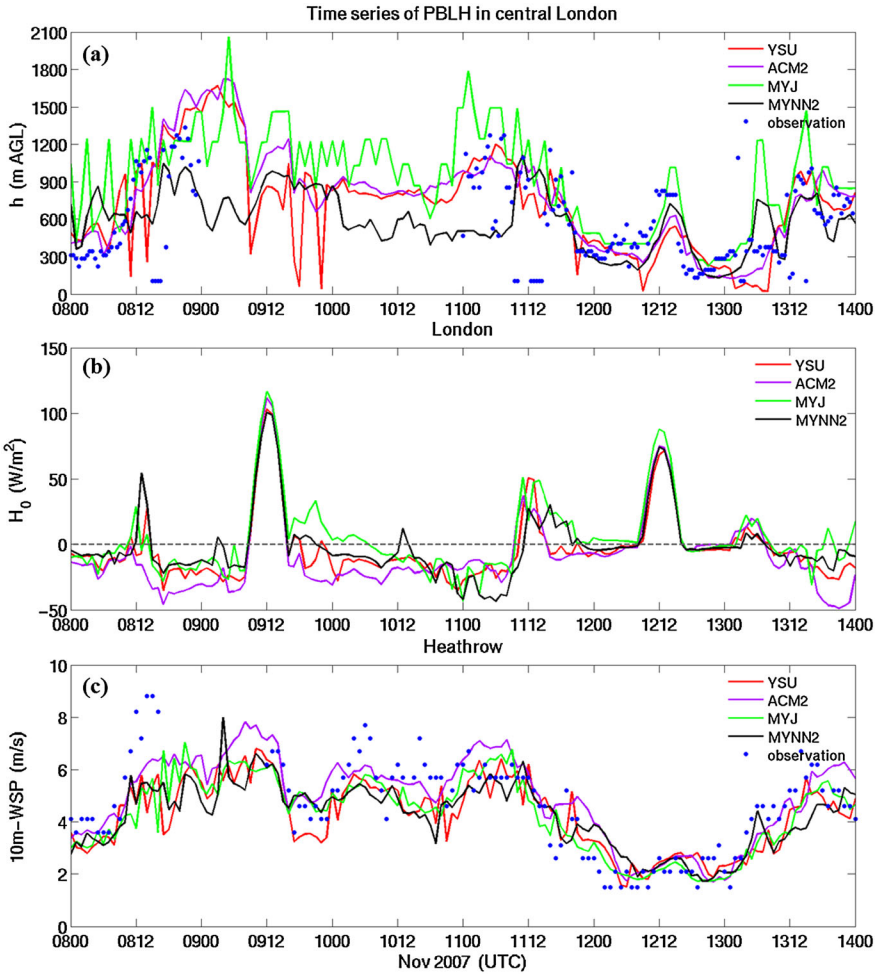


**Figure 7.** (a) PBL height in central London, (b) surface sensible heat flux in London, and (c) 10 m wind speed at Heathrow from 8 to 14 November.

surface should produce TKE that is at least larger than the minimum in this case.

[29] The MYNN2 PBL scheme can also overestimate the entrainment layer depth. On 3 November, MYNN2 diagnoses an even higher PBL top at 610 m AGL (Figure 6a) than MYJ. In MYNN2, the PBL height $h_\theta$, computed using the theta-increase method by equation (14), is about 250 m AGL, leading to $w_f = 0.56$ in equation (16). The PBL height $h_e$, computed with the TKE method by equation (15), is about 1100 m AGL, where the $TKE_{cr}$ equals to 0.025 $m^2/s^2$ in this case. The PBL height is then blended by equation (17), which has two problems. First, the large difference between $h_\theta$ and $h_e$ implies that they are not suitable to be blended. Second, equation (16) gives too much weight to the TKE method, producing a blended $h$ that is much higher than the inversion base (about 170 m AGL) in this case. Since the TKE method was designed for estimating the PBL height in low-level jets, it should contribute much less to the weighting function equation (16) in unstable conditions, where no low-level jets exhibit. On the other hand, the relatively large TKE predicted by MYNN2 (Figure 6b) above the inversion base, where the wind shear is weak in this case, appears unphysical and is related to the increase in the turbulent length scale. This is discussed in detail in section 4.5. On 16 November, the theta-increase and TKE methods in MYNN2 diagnose similar PBL heights. The difference between the PBL height diagnosed by MYNN2 and those diagnosed by the nonlocal PBL schemes (Figure 6c) can mainly be explained by the virtual potential temperature excess. The value of 1.5 in equation (14) for the temperature excess in MYNN2 may be somewhat simplistic in not taking account of different stability conditions as parameterized by equation (11) in the nonlocal PBL schemes.

[30] Unrealistic high-frequency oscillations of the PBL height are predicted in YSU and MYJ, as shown in Figure 7a. The oscillation of the PBL height in YSU (e.g., an oscillation magnitude of 1000 m from 10 A.M. to 4 P.M. on 8 November and from 10 A.M. on 9 November to 0 A.M. on 10 November in Figure 7a) occurs when the predicted surface kinematic heat flux varies between positive and negative. As the surface moisture flux is very small in this case, the sign of the surface heat flux depends on the surface sensible heat flux (Figure 7b). In stable conditions, the diagnostic formulation of $h$ in YSU is dependent on the bulk temperature gradient $[\theta_v(z) - \theta_v(z_1)]$ and the wind speed $U(z)$ in equation (9), but in unstable conditions, the diagnostic formulation is only dependent on the bulk temperature gradient $[\theta_v(z) - \theta_s]$ since in equation (10) $Ri_b = Ri_{bcr} = 0$ at the PBL top. Therefore, the transition between stable and unstable regimes in the YSU PBL scheme is not continuous, especially

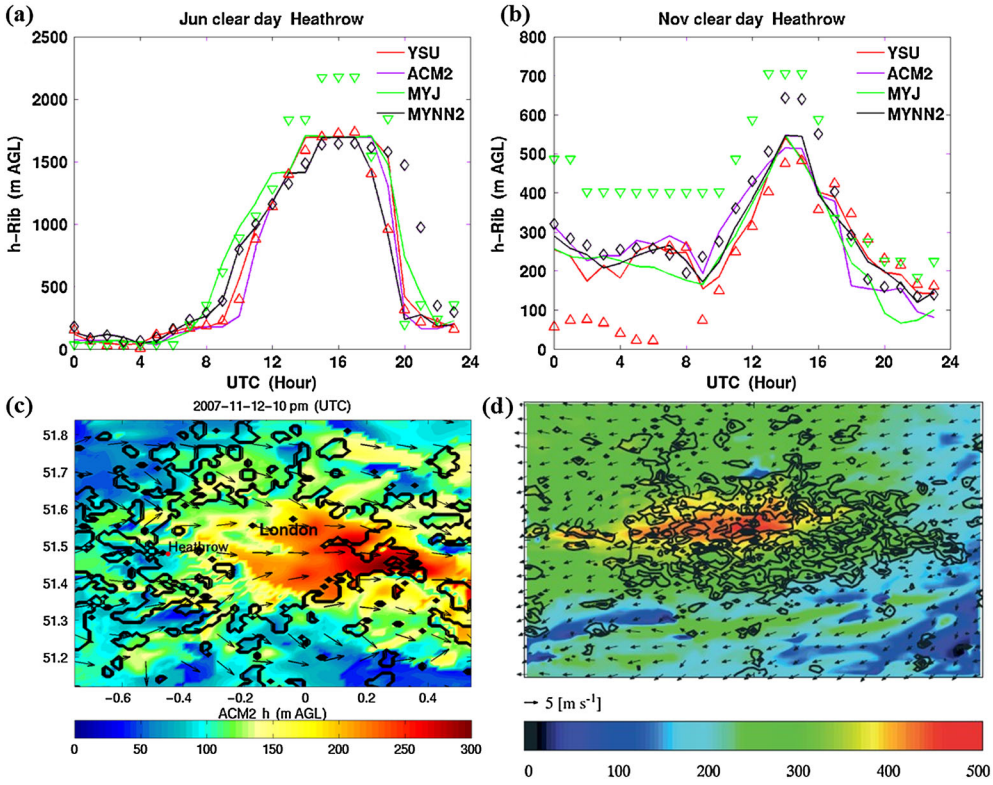


**Figure 8.** PBL height on clear days of (a) 2 June and (b) 12 November (symbols: predictions by each PBL scheme; solid lines: diagnoses by the bulk Richardson number method); PBL height over Greater London (c) at 10 P.M. on 12 November 2007 from ACM2 predictions in WRF and (d) at 10 P.M. on 7 May 2008 from simulations of *Bohnenstengel et al.* [2011] (black contours circumscribe the urban grids area, and black vectors indicate the 10 m wind vectors).

when the wind shear is strong (e.g., when 10 m wind speed exceeds 4 m/s as shown in Figure 7c for Heathrow). The oscillation of a few hundred meters of $h$ in MYJ (Figure 7a) is related to the minimum TKE method and the vertical grid spacing. Since MYJ diagnoses the PBL height at a model layer where the TKE decreases to the minimum value, the values of $h$ are discrete and exhibit steps dependent on the model's vertical grid spacing, which near the convective PBL top (e.g., 1500 m AGL) is typically a few hundred meters. This unphysical diagnosis of $h$ in MYJ could be improved by modifying the critical TKE value to be larger than a set minimum value and interpolating the TKE between the model layers.

#### 4.3.3. Observed Boundary Layer Height and Wind Shear in London

[31] The blue dots in Figure 7a show the PBL height observed by the lidar in London from 8 to 14 November 2007. Although this period exhibits variable cloud cover, the comparison focuses on the high values of $h$ during the nighttime. The observed PBL height is determined as the height at which the vertical velocity variance measured by the lidar drops below a critical value ($\overline{w'^2} < 0.1\ \mathrm{m^2/s^2}$). Values of $h$ below 90 m AGL, which cannot be measured by the lidar, have been filtered out. The high values of $h$ above 1000 m AGL on the night of 8 November and on the early morning of 11 November (Figure 7a) are observed from the lidar data and also captured by the simulations. This indicates that when the wind shear is very strong at nighttime (e.g., when 10 m wind speed exceeds 4 m/s as shown in Figure 7c for Heathrow), the shear turbulence can contribute to a deep PBL, even though the surface sensible heat flux is downward (Figure 7b) and the PBL is stably stratified. The purely thermal methods such as equation (14) cannot produce this high PBL height under stable conditions. Note that in *Harrison et al.* [2012], a value of $h$ as low as 200 m was recorded during several nights. It can be seen from Figure 7a that the PBL height predicted by ACM2 using the bulk Richardson number method does not have the oscillation problem and shows a good agreement with the lidar observations for both stable and unstable conditions.

#### 4.3.4. Boundary Layer Height Rediagnosed by the Bulk Richardson Number Method Under a Clear Sky

[32] Due to the disparate definitions of the PBL top in each PBL scheme and the formulation limitations in YSU, MYJ, and MYNN2 as discussed above, the PBL heights on the clear days in June and November at Heathrow were rediagnosed by the bulk Richardson number method as used in ACM2. The solid lines in Figures 8a and 8b represent the rediagnosed PBL heights, and the symbols represent the diagnoses by each PBL scheme. The spreads in the solid lines are much smaller than that in the symbols, which implies the differences in the PBL heights diagnosed by each PBL scheme are primarily due to the disparate definitions. As MYJ and MYNN2 can diagnose an unrealistically large vertical extent between the mixed layer top and the PBL

**Table 3.** Ensemble Average of YSU, ACM2, and MYNN2 Predictions

| Clear Days | 2 June | | | | 12 November | | | |
|---|---|---|---|---|---|---|---|---|
| Hour | Daytime (2 P.M.) | | Nighttime (2 A.M.) | | Daytime (2 P.M.) | | Nighttime (2 A.M.) | |
| Sites | Heathrow (urban) | Andrewsfield (rural) | Heathrow (urban) | Andrewsfield (rural) | Heathrow (urban) | Andrewsfield (rural) | Heathrow (urban) | Andrewsfield (rural) |
| $w_*$ (m/s) | 2.35 | 1.67 | 0 | 0.24 | 0.97 | 0.59 | 0.29 | 0 |
| $u_*$ (m/s) | 0.53 | 0.3 | 0.1 | 0.1 | 0.49 | 0.43 | 0.49 | 0.43 |
| $w_*/u_*$ | 4.4 | 5.6 | 0 | 2.4 | 2.0 | 1.4 | 0.6 | 0 |
| $h/L$ | −34.2 | −68.0 | 0.96 | −5.2 | −3.2 | −1.1 | −0.1 | 1.0 |

top and YSU can lead to an oscillation in the PBL height (discussed in section 4.3.2), the bulk Richardson number method in ACM2 is more physical by considering both thermals and wind shear and produces PBL heights that agree well with observations (Figure 7a).

[33] Figure 8c depicts the PBL height predicted by ACM2 over Greater London at 10 P.M. on 12 November. The sky was clear across Greater London. An urban PBL formed and increased in depth with urban fetch towards the eastern side of Greater London. In the evening, the prevailing wind over London changed from a northwest to a west flow after 9 P.M. Therefore, the western part of London formed the upwind edge of London and the PBL was shallower over that part of the city. The spatial variability of a shallower PBL depth in the upwind edge and a greater PBL depth in the downwind edge of London resemble the simulations of *Bohnenstengel et al*. [2011] using the UK Met Office Unified Model (Figure 8d).

### 4.4. Convective Velocity Scale $w_*$, Friction Velocity $u_*$, and Dimensionless Length Scale $h/L$ Under a Clear Sky

[34] The convective velocity scale $w_*$, the friction velocity $u_*$, and the dimensionless length scale $h/L$ on the clear days were compared for the different PBL schemes (not shown). Values of $w_*$, $u_*$, and $h/L$ predicted by YSU, ACM2, and MYNN2 are broadly similar. However, MYJ predicts comparatively higher values of $w_*$ and $-h/L$ in the daytime due to its surface sensible heat fluxes (Figures 5a and 5b) related to the $C_h$ (Figures 5e and 5f) and its higher diagnostic values of $h$ (Figures 8a and 8b). In order to estimate the representative values of $w_*$, $u_*$, $w_*/u_*$, and $h/L$ over the urban and rural grids for the clear days in June and November, ensemble averages of these quantities in Table 3 were calculated using the predictions from the runs with the YSU, ACM2, and MYNN2 PBL schemes. The MYJ predictions are not included because they are markedly different for $w_*$ and $h/L$.

[35] $w_*$ is defined as $w_* = \left[\frac{gh\overline{(w'\theta_v')}_o}{\theta_v(z_1)}\right]^{1/3}$, where $\overline{(w'\theta_v')}_o \geq 0$ (18)

[36] On the clear days, $w_*$ over the urban grid (Heathrow) is larger than that over the rural grid (Andrewsfield) during the daytime, inducing more turbulence if the TKE is parameterized with $w_*$. During the daytime for the clear day in June, the simulated value of $w_*$ is about 5 times the value of $u_*$, showing the dominance of convective mixing. During the daytime for the clear day in November, the ratios $w_*/u_*$ are 2.0 over the urban grid and 1.4 over the rural grid so that the convective mixing is less dominant and the shear turbulence has more influence. It is notable that during the daytime for the clear day in June, the predicted value of $-h/L$ can be larger over the rural grid than over the urban grid. This is primarily due to the much smaller $u_*$ predicted over the rural grid, giving rise to a larger $L^{-1}$ that is proportional to $u_*^{-3}$ in equation (1). The values of $h/L$ are used to define the strongly convective, weakly convective and near-neutral PBL in the next section.

### 4.5. Vertical Profiles in the Strongly Convective, Weakly Convective, and Near-Neutral PBL

[37] The modeled vertical profiles of potential temperature $\theta$, wind speed, eddy diffusivity, turbulent length scale, TKE, and heat flux as functions of the normalized height $z/h$ in the strongly convective ($-h/L \approx 34$), weakly convective ($-h/L \approx 3$), and near-neutral ($-h/L \approx 0.3$) PBL are depicted in Figures 9–11, where the PBL heights are diagnosed by each PBL scheme. In addition to the clear days on 2 June and 12 November, the PBL at 2 P.M. on another clear day (9 November) at Andrewsfield is included (Figure 11). This near-neutral PBL exhibits a low value of $-h/L$ with weak surface heating and relatively strong wind. The simulated values of $h/L$ are similar across the PBL schemes except MYJ for the three convective cases under clear skies.

[38] Displayed in Figure 9a for the strongly convective PBL, the local PBL schemes exhibit negative gradients $\partial\theta/\partial z$ throughout the mixed layer below the inversion base, whereas the nonlocal PBL schemes exhibit zero or slightly positive gradients $\partial\theta/\partial z$. The unstable profiles of $\theta$ in the mixed layer produced by MYJ and MYNN2 are attributable to the problem of the turbulence being parameterized as down-gradient throughout the PBL. The $\theta$ profiles need to be slightly unstable in order to transport heat and moisture upward, as nonlocal mixing is not permitted in these local PBL schemes [*Hong and Pan*, 1996; *Nakanishi and Niino*, 2009]. The wind profiles simulated by the nonlocal PBL schemes are more well-mixed in the PBL interior than those simulated by the local PBL schemes (Figure 9b).

[39] Figure 9c depicts the dimensionless eddy diffusivity $K_h$ normalized by the turbulent velocity scale for heat $w_t$ and the PBL height $h$. In both the YSU and ACM2 PBL schemes, the eddy diffusivity is parameterized as

$$K_h = \kappa w_t z\left(1 - \frac{z}{h}\right)^2 \quad (19)$$

although they differ in their parameterizations of $w_t$. $w_t$ in the

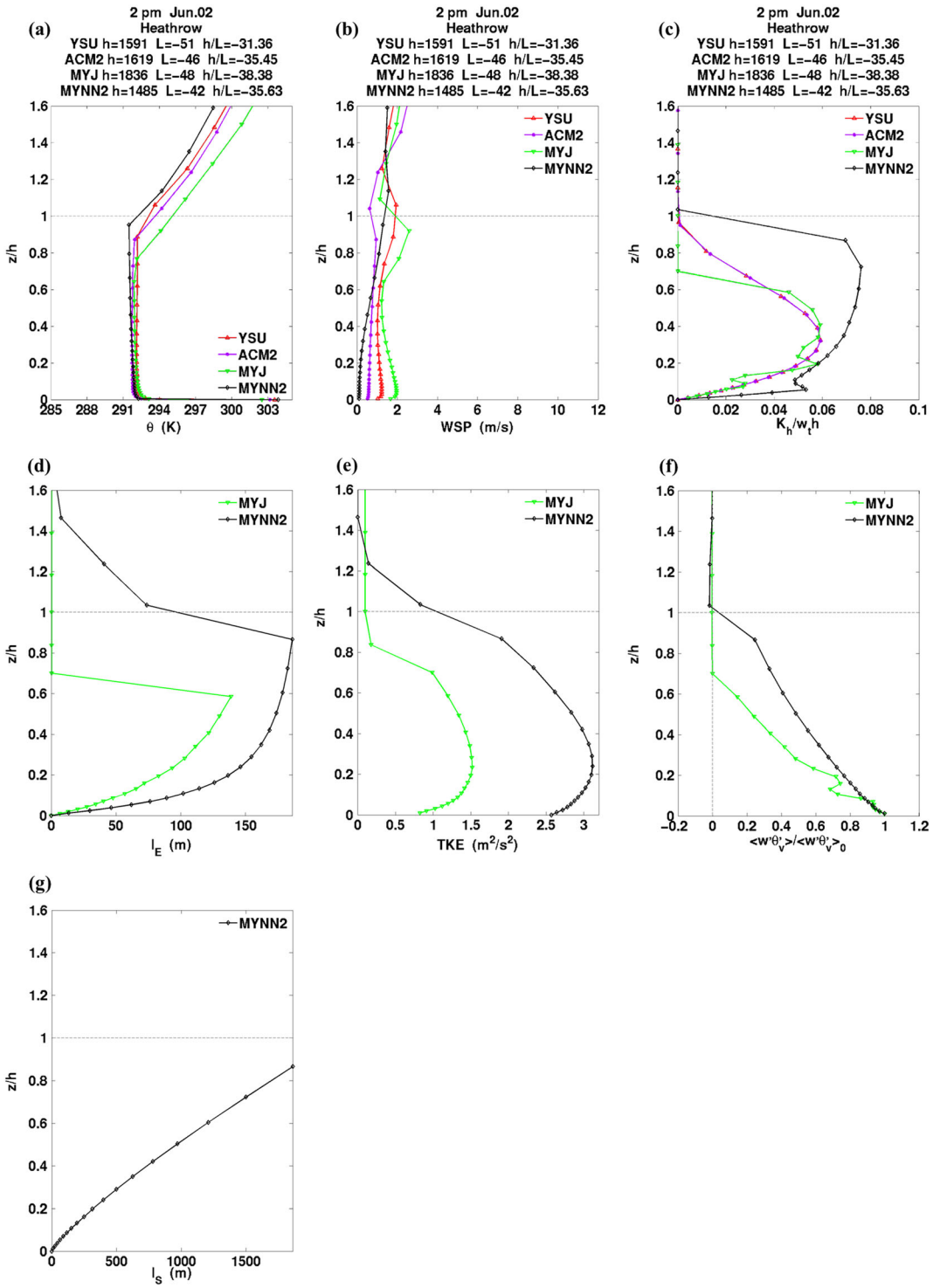


**Figure 9.** Vertical profiles of (a) potential temperature, (b) wind speed, (c) normalized eddy diffusivity, (d) turbulent length scale, (e) TKE, (f) normalized kinematic heat flux, and (g) length scale in the surface layer at Heathrow at 2 P.M. on 2 June 2007 for the strongly convective PBL.

YSU PBL scheme is defined as the turbulent velocity scale for momentum divided by the Prandtl number. Since we are interested in the profile shape of the dimensionless eddy diffusivity $K_h/w_t h$, we adopted the simpler definition of $w_t$ as used in the ACM2 PBL scheme to normalize the eddy diffusivities predicted by the local PBL schemes MYJ and MYNN2.

$$w_t = \frac{u_*}{\phi_h} \tag{20}$$

where $\phi_h = \left(1 - 16\frac{z_*}{L}\right)^{-1/2}$ is the dimensionless stability

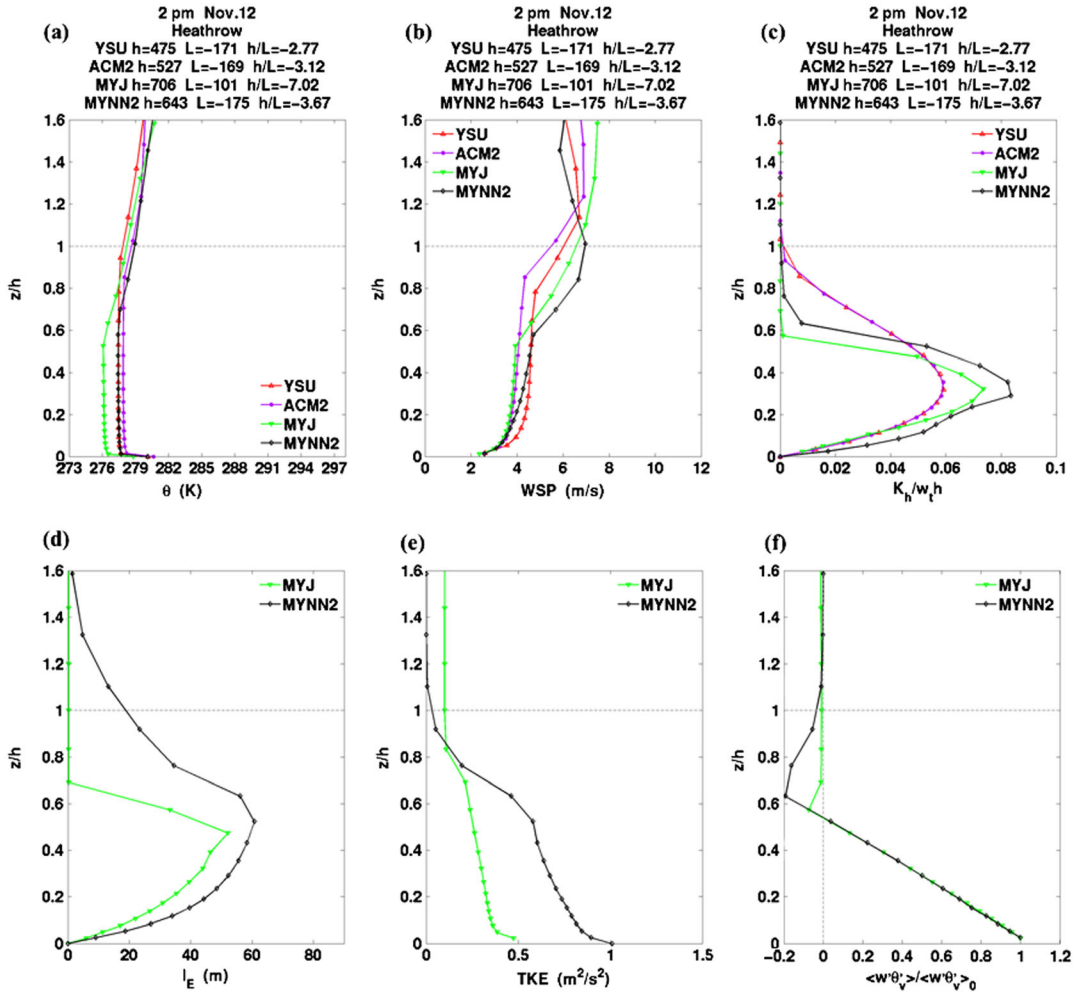


**Figure 10.** Vertical profiles of (a) potential temperature, (b) wind speed, (c) normalized eddy diffusivity, (d) turbulent length scale, (e) TKE, and (f) normalized kinematic heat flux at Heathrow at 2 P.M. on 12 November 2007 for the weakly convective PBL.

function for heat and $z_s = \min(z,\ 0.1h)$. Therefore, the normalized eddy diffusivities for the YSU and ACM2 PBL schemes employ the same equation

$$\frac{K_h}{w_t h} = \frac{\kappa z}{h}\left(1 - \frac{z}{h}\right)^2 \tag{21}$$

whereas the normalized eddy diffusivities for MYJ and MYNN2 were computed with $w_t$ in equation (20) and their own diagnosed PBL heights. Note that the eddy diffusivities are used differently in the prognostic equations across the PBL schemes and that ACM2 uses another parameterization based on the Richardson number for the eddy diffusivity near the PBL top. The evaluation here therefore focuses on comparing the shapes and magnitudes of the normalized eddy diffusivities. Figure 9c shows that the normalized eddy diffusivity predicted by MYNN2 is higher than the other PBL schemes above 0.3 $h$. It increases with height and peaks at about 0.75 $h$. This increase as in equation (6) is due to the increase in the turbulent length scale, which should decrease in the upper part of the convective PBL. The turbulent length scale $l_E$ in the MYNN2 PBL scheme is parameterized as

$$\frac{1}{l_E} = \frac{1}{l_S} + \frac{1}{l_T} + \frac{1}{l_B} \tag{22}$$

[40] $l_E$ is designed to be controlled by the smallest length scale among the three length scales $l_S$, $l_T$, and $l_B$. $l_S$ is the length scale in the surface layer. $l_T$ is the length scale dependent on the PBL depth and is independent of height. $l_B$ is related to the buoyance length scale $q/N$, where $N$ is the Brunt-Väisälä frequency, and is effective only in a stable layer, i.e., $l_B = \infty$ when $\partial\theta_v/\partial z \le 0$ [*Nakanishi and Niino*, 2009]. In the convective PBL ($L < 0$),

$$l_S = \kappa z\left(1 - c_1\frac{z}{L}\right)^{0.2} \tag{23}$$

where the constant $c_1$ is adjusted to 20 in WRF version 3.4.1 from 100 determined in *Nakanishi and Niino* [2009]. For this strongly convective PBL, $l_T \approx$ 190 m. The smaller $c_1$ increases the weighting of $l_S$ in equation (22). Therefore, in the upper part of the convective PBL, where MYNN2 predicts $\partial\theta_v/\partial z \le 0$ (similar to $\partial\theta/\partial z$ in Figure 9a) and $l_B = \infty$, $l_S$ (Figure 9g) determines that $l_E$ (Figure 9d) increases with height. However, this increase is unexpected and conflicts

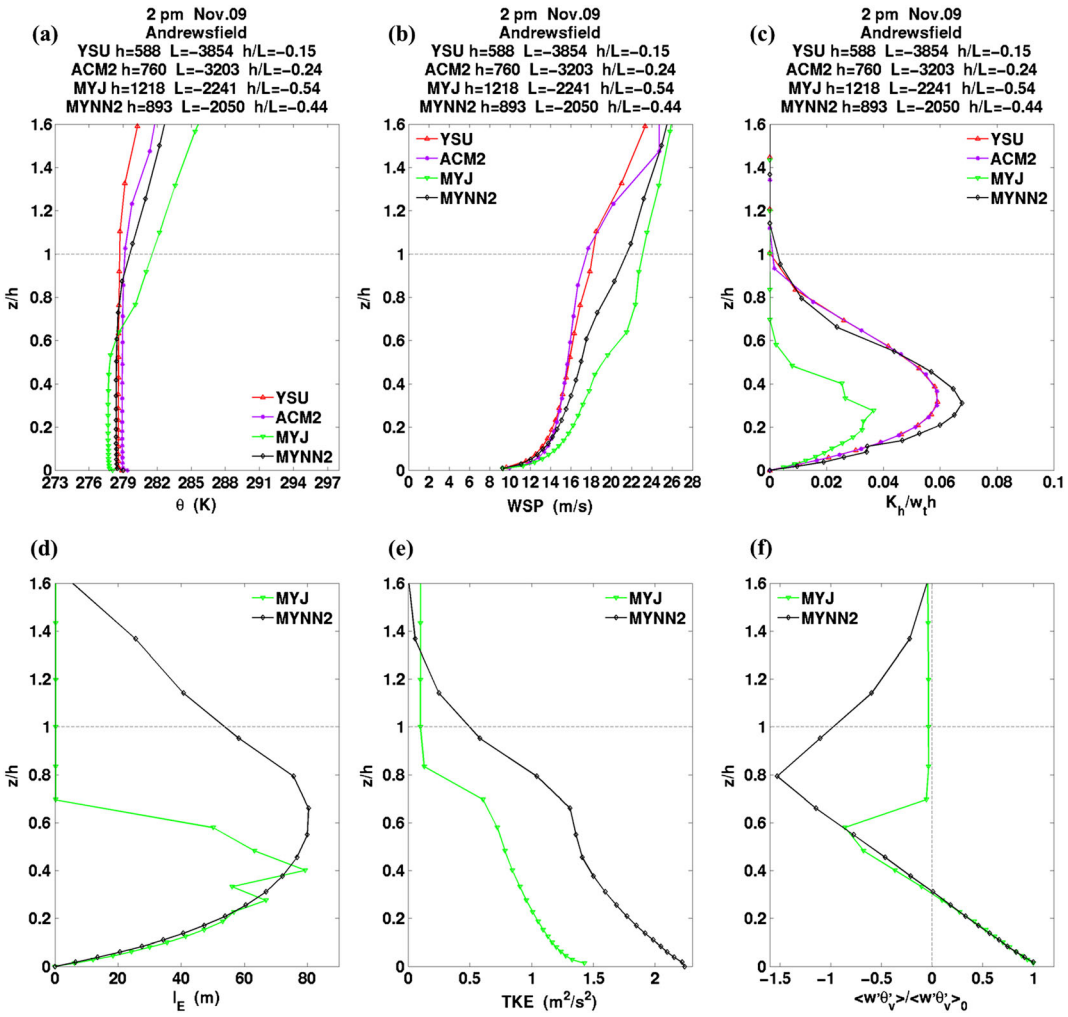


**Figure 11.** Same as Figure 10 but for Andrewsfield at 2 P.M. of 9 November 2007 for the near-neutral PBL.

with the current theory. Nevertheless, MYNN2 predicts a larger turbulent length scale $l_E$ throughout the PBL than MYJ (Figure 9d), which primarily produces a larger TKE (Figure 9e) [*Nakanishi and Niino*, 2009]. The MYNN2 eddy diffusivity decreases to almost zero near the PBL top (Figure 9c) due to the stability function for heat $S_h$ in equation (6), leading to a near-zero kinematic heat flux (Figure 9f), where the gradient $\partial\theta_v/\partial z > 0$. The near-zero entrainment/surface flux ratios modeled by MYNN2 and MYJ near the PBL top (Figure 9f) do not fit with the LES results of *Moeng and Sullivan* [1994], where the entrainment/surface flux ratio can be represented as

$$\frac{\overline{(w'\theta_v')}_i}{\overline{(w'\theta_v')}_0} = -0.2 - \frac{T_0 u_*^3}{gh\overline{(w'\theta_v')}_0} \approx -0.2 - \kappa\left(-\frac{h}{L}\right)^{-1} \qquad (24)$$

[41] $\overline{(w'\theta_v')}_i$ denotes the minimum kinematic heat flux at the capping inversion layer. Therefore, the ratio $\overline{(w'\theta_v')}_i/\overline{(w'\theta_v')}_0$ in equation (24) should be −0.2 for a free convective PBL and smaller than −0.2 for a shear convective PBL. The near-zero ratios modeled by MYJ and MYNN2 are considerable underestimates.

[42] The wind speed profiles produced by the nonlocal PBL schemes exhibit more unstable shapes than the local PBL schemes for the weakly convective (Figure 10b) and near-neutral (Figure 11b) PBL. The more well-mixed wind profiles for the weakly convective PBL (Figure 10b) simulated by the nonlocal PBL schemes resemble the cases ($-h/L = 4.5$ and $-h/L = 1.5$) presented by *Deardorff* [1972]. *Moeng and Sullivan* [1994] also observed that a small amount of buoyancy forcing is sufficient to create a mixed layer in the mean wind field based on their SB1 and SB2 LES simulations ($-h/L \approx 1.5$). As shown in Figures 10c and 11c, the normalized eddy diffusivities modeled by the local PBL schemes exhibit similar U curves which are narrower than the nonlocal PBL schemes. The normalized eddy diffusivities modeled by MYNN2 exhibit larger peak magnitudes than the others for the weakly convective and near-neutral PBL. The peak magnitude of the eddy diffusivity modeled by MYJ is significantly lower than the others for the near-neutral PBL (Figure 11c). The near-zero values of the normalized eddy diffusivities at about 0.7 $h$ modeled by MYJ (Figures 10c and 11c) are consistent with that its minimum TKE method yielding an unrealistically high PBL height in November across SE England, as discussed in section 4.3.2. The turbulent length scales

**Table 4.** Entrainment/Surface Flux Ratios

| PBL Schemes | MYJ | | | MYNN2 | | |
|---|---|---|---|---|---|---|
| Entrainment/Surface Flux Ratio | Modeled | Equation (24) With MYJ-Diagnosed PBL Height $h$ | Equation (24) With the PBL Height Defined by the Minimum Heat Flux $h_{mhfx}$ | Modeled | Equation (24) With MYNN2-Diagnosed PBL Height $h$ | Equation (24) With the PBL Height Defined by the Minimum Heat Flux $h_{mhfx}$ |
| Strongly Convective PBL | −0.0018 | −0.2101 | −0.2121 ($h_{mhfx}=0.84h$) | −0.0168 | −0.2103 | −0.2100 ($h_{mhfx}=1.04h$) |
| Weakly Convective PBL | −0.07 | −0.26 | −0.30 ($h_{mhfx}=0.57h$) | −0.19 | −0.31 | −0.37 ($h_{mhfx}=0.63h$) |
| Near-Neutral PBL | −0.86 | −0.86 | −1.34 ($h_{mhfx}=0.58h$) | −1.53 | −1.03 | −1.25 ($h_{mhfx}=0.79h$) |

modeled by MYNN2 are larger than MYJ throughout the PBL for the weakly convective PBL (Figure 10d) and above 0.4 $h$ for the near-neutral PBL (Figure 11d). The TKE values predicted by MYNN2 are larger than MYJ throughout the PBL (Figures 10e and 11e). The TKE predictions will be further discussed in section 4.6.

[43] The entrainment/surface flux ratios computed by equation (24) for all three convective cases are summarized in Table 4. For the strongly convective and weakly convective PBL, the computed ratios indicate that both MYJ and MYNN2 significantly underestimate the entrainment fluxes. The PBL height ($h_{mhfx}$) in the LES study is defined as the height at which the minimum heat flux exists [*Moeng and Wyngaard*, 1989; *Moeng and Sullivan*, 1994]. $h_{mhfx}$ in MYJ and MYNN2 are very close to those rediagnosed by the bulk Richardson number method, and they are lower than those defined by the diagnostic formulations of MYJ and MYNN2, as shown in Figures 10f and 11f. This strengthens the conclusion that the entrainment layer depths are overestimated by MYJ and MYNN2. In Table 4, the

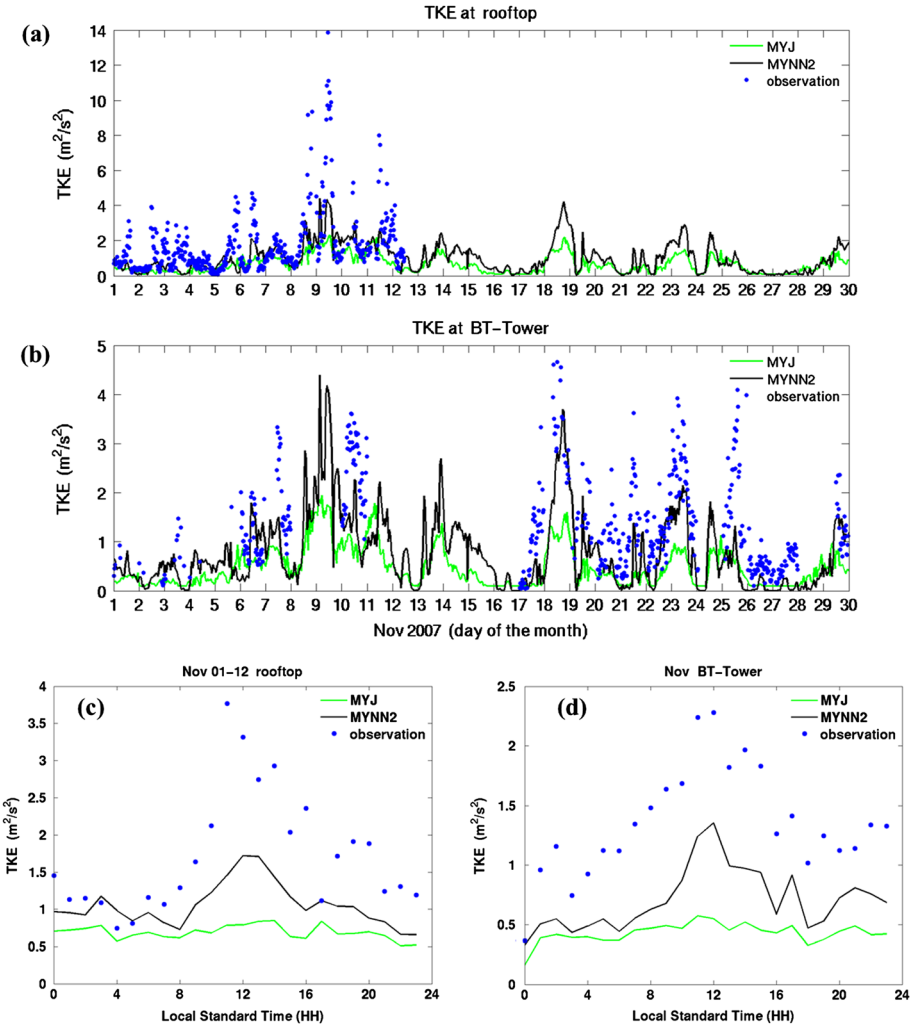


**Figure 12.** TKE predicted by MYJ and MYNN2 and observed TKE (blue dots) from 1 to 30 November at (a) rooftop and (b) BT Tower; mean diurnal TKE in November at (c) rooftop and (d) BT Tower in central London.

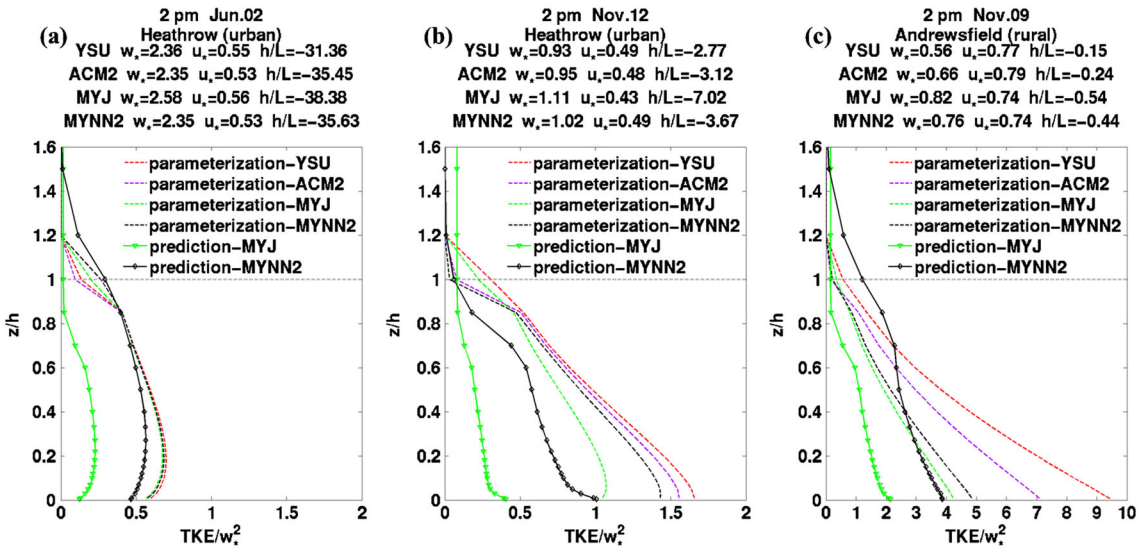


**Figure 13.** Vertical profiles of TKE for the (a) strongly convective PBL, (b) weakly convective PBL, and (c) near-neutral PBL (solid lines represent TKE predicted by MYJ and MYNN2; dashed lines represent TKE parameterized following equations (25)–(27) with $u_*$, $w_*$, and $h$ modeled by each PBL scheme).

entrainment/surface flux ratio computed with $h_{mhfx}$ in the weakly convective PBL for MYNN2 ($-h_{mhfx}/L = 2.3$) is $-0.37$, which is close to the value of $-0.5$ in the SB1 and SB2 LES simulations ($-h/L \approx 1.5$) of *Moeng and Sullivan* [1994]. The ratio computed with $h_{mhfx}$ indicates that MYJ also underestimates the entrainment flux for the near-neutral PBL.

### 4.6. Turbulent Kinetic Energy

[44] The TKE measured every 30 min at the rooftop and the BT Tower sites in central London in November were compared with the modeled TKE. The TKE values at the rooftop were measured before mid-November, and the TKE values at the BT Tower were patchy before mid-November but available after mid-November. The sonic anemometer used to measure TKE is mounted at 2 m above rooftop (17 m AGL). Therefore, the rooftop observations were compared with the modeled TKE at the lowest full sigma level (about 17.5 m AGL). The BT Tower observations (190 m AGL) were compared with the simulations at the ninth full sigma level (about 198 m AGL). Note that because the rooftop site in central London may be within the urban canopy layer, one should expect limitations in the predictions since buildings are not modeled explicitly [*Chan et al.*, 2013; *Ng et al.*, 2011].

[45] The TKE are predicted by the local TKE PBL schemes MYJ and MYNN2. In Figure 12a, the modeled TKE are much lower than the observations at the rooftop. This may be due to the fact that the considerable shear and/or buoyancy production of TKE at the rootop within the urban canopy layer are underestimated by the two PBL schemes. Nevertheless, MYNN2 produces TKE values that are twice as large as those produced by MYJ during the daytime, as shown in Figures 12a and 12c. At the BT Tower, the larger TKE values predicted by MYNN2 are in much closer agreement with the observations than MYJ. The flat diurnal variations of the TKE values predicted by MYJ at both the rooftop (Figure 12c) and the BT Tower (Figure 12d) indicate that the buoyancy production of TKE during the daytime with surface heating may not be well parameterized by MYJ. The better agreement with observations and stronger diurnal variations of the TKE predicted by MYNN2 imply that the modifications in the turbulent length scale and TKE prognostic equations improve the TKE predictions at low levels over the MYJ PBL scheme.

[46] It is interesting to compare the turbulence structure in the PBL predicted by WRF with that of a one-dimensional boundary layer model [e.g., *Driedonks*, 1982; *Nieuwstadt*, 1981] such as that used in the Atmospheric Dispersion Modeling System (ADMS) [*Hunt et al.*, 1988b; *Carruthers et al.*, 1994]. The ADMS is a Gaussian plume air dispersion model that simulates a wide range of buoyant and passive releases to the atmosphere. It uses the PBL height $h$ and the Monin-Obukhov length $L$ to describe the PBL and a skewed Gaussian concentration distribution to calculate dispersion under convective conditions. The TKE values predicted by MYJ and MYNN2 were compared with those parameterized with the modeled $u_*$ and $w_*$ following well-established equations [e.g., *Lenschow et al.*, 1980; *Hunt et al.*, 1988a] as used in the ADMS. *Hunt et al.* [1988b] parameterizes the velocity variances $\overline{u'^2}$, $\overline{v'^2}$, and $\overline{w'^2}$ according to the ranges of $h/L$; however, due to the uncertainty in estimating $h$ across different PBL schemes, we used TKE parameterizations similar to those of *Hunt et al.* [1988b] but categorized only by the Monin-Obukhov length $L$. The constant 0.8 in equations (25) and (26) is empirically based [*Lenschow et al.*, 1980].

[47] In unstable conditions ($L < 0$),

$$\overline{u'^2} = \overline{v'^2} = 0.3w_*^2 + 4.0u_*^2\left(1 - 0.8\frac{z}{h}\right)^2 \tag{25}$$

$$\overline{w'^2} = 1.764w_*^2\left(\frac{z}{h}\right)^{2/3}\left(1 - 0.8\frac{z}{h}\right)^2 + 1.69u_*^2\left(1 - 0.8\frac{z}{h}\right)^2 \tag{26}$$

$$TKE = \frac{\overline{u'^2} + \overline{v'^2} + \overline{w'^2}}{2} \tag{27}$$

[48] In Figure 13, the vertical profiles of TKE are normalized by $w_*^2$ for dimensionless analysis. The dashed red,

purple, green, and black lines represent the normalized TKE parameterized following equations (25)–(27) with $u_*$, $w_*$, and $h$ modeled by YSU, ACM2, MYJ, and MYNN2, respectively. The solid green and black lines represent the TKE predicted by MYJ and MYNN2, respectively. The TKE values predicted by MYJ are much lower than those predicted by MYNN2 and those parameterized for the strongly convective (Figure 13a), weakly convective (Figure 13b), and near-neutral (Figure 13c) PBL. The vertical profiles of the normalized TKE in the strongly convective PBL (Figure 13a) exhibit prominent maxima near the surface because of the vertical component, as did the observations of *Caughey and Palmer* [1979]. The normalized TKE monotonically decrease with height in both the weakly convective (Figure 13b) and near-neutral (Figure 13c) PBL. Note that in Figure 13c, the normalized TKE parameterized with YSU (dashed red line) are higher than those parameterized with the other PBL schemes because the $u_*/w_*$ predicted by YSU is higher. The larger TKE predicted by MYNN2 and that parameterized by equations (25)–(27) for the three cases strengthen the conclusion that MYJ underpredicts TKE. Note that there are other ways to enhance the TKE predictions from MYJ; for example, *Foreman and Emeis* [2012] modified the closure constants and the surface length scale in MYJ and obtained larger TKE predictions that are closer to the observations. Those suggested modifications for the Mellor-Yamada model will be evaluated against LES results and observations over different stability conditions in a future study.

## 5. Conclusions

[49] This study evaluates the parameterizations and prognostic skills of the nonlocal and local mixing PBL schemes in the WRF model over various stability conditions in the mid-high latitude region of SE England in the UK. To avoid further uncertainties associated with the simulated cloud cover, particularly modeling radiation, the study focuses on the PBL structures under clear skies. The nonlocal PBL schemes YSU and ACM2 predict a more realistic eddy structure of the convective PBL. The PBL heights, estimated by scheme-specific formulations, exhibit more than 20% variance. ACM2 presents a physical diagnosis of the PBL height using the bulk Richardson number method above the surface for stable conditions and over the stable entrainment layer for unstable conditions. The specific points from our study are as follows.

[50] 1. In June, the differences in 2 m temperature and 10 m wind among the simulations with different PBL schemes are relatively small. In November, the cloud cover and insolation may not be well modeled, as all the PBL schemes underestimate the daytime 2 m temperatures. Nevertheless, the nonlocal PBL scheme ACM2 exhibits better 2 m temperature and 10 m wind predictions than the other PBL schemes as compared with the measurements across SE England.

[51] 2. The Eta-similarity surface layer scheme, which is tied to the MYJ PBL scheme, produces stronger mixing in the surface layer with a larger heat exchange coefficient $C_h$ and a smaller near-surface temperature gradient in the daytime compared with the MM5-similarity surface layer scheme. The larger $C_h$ yields a larger surface sensible heat flux, a lower surface skin temperature, and a higher 2 m temperature in the MYJ-Eta run in June, but a lower 2 m temperature in November when the near-surface temperature gradient is smaller. The large underestimation in 2 m temperature in the MYJ-Eta run in November is partly attributable to the Eta-similarity surface layer scheme.

[52] 3. The observations and WRF simulations both show that in stably stratified but windy conditions (e.g., 10 m wind speed $> 4$ m/s), shear turbulence can produce PBL heights of greater than 1000 m AGL in SE England. It is also shown in this study and in the simulations by *Bohnenstengel et al.* [2011] and *Hunt et al.* [2012] that the nocturnal PBL heights over Greater London vary spatially with the prevailing flow. As the thermal plume extends towards the downwind edge of the city, the urban PBL depth increases.

[53] 4. The MYJ minimum TKE method and the MYNN2 hybrid method can diagnose PBL heights that are much higher than the inversion base for the convective PBL, especially for the weakly convective PBL in November. The oscillation of the PBL height in YSU in the neutral windy conditions stems from the discontinuous transition of the diagnostic formulations from unstable to stable conditions. The discrete form and oscillation of the PBL height in MYJ are related to the minimum TKE method and the vertical grid spacing. The PBL heights rediagnosed by the bulk Richardson number method show much smaller spreads and imply the differences in the PBL heights are mainly caused by the disparate definitions across the PBL schemes.

[54] 5. The unstable profiles of $\theta$ in the upper part of the convective PBL modeled by MYJ and MYNN2 exhibit the well-known problem of down-gradient-parameterized turbulence in the local PBL schemes. The eddy diffusivity modeled by MYNN2 increases in the upper part of the convective PBL due to the unphysical increase of the turbulent length scale, as parameterized by equations (22) and (23). The turbulent length scale should be modified to decrease with height in the upper part of the convective PBL.

[55] 6. The more well-mixed wind profiles modeled by the nonlocal PBL schemes for the strongly convective, weakly convective, and near-neutral PBL agree with the LES results of previous studies and corroborate the conclusion that a small amount of buoyancy is sufficient to create a mixed layer in the mean field.

[56] 7. The entrainment/surface flux ratios estimated by equation (24) from *Moeng and Sullivan* [1994] indicate that the entrainment fluxes are underestimated by MYJ and MYNN2 for the strongly convective and weakly convective PBL.

[57] 8. The observed TKE in November, the MYNN2 predictions, and the parameterized TKE following equations (25)–(27) such as that in the ADMS model, all indicate MYJ considerably underestimates TKE in both June and November. Compared with the observations and MYNN2 predictions, the flat diurnal variations in the MYJ TKE predictions imply that the buoyancy production of TKE is not well parameterized by MYJ. The vertical profiles of the modeled and parameterized TKE exhibit maxima near the surface for the convective PBL, which agree with the observations of *Caughey and Palmer* [1979].

[58] The local TKE PBL schemes which do not consider large-scale eddies are insufficient for modeling the convective PBL [*Hunt et al.*, 1988a; *Moeng and Sullivan*, 1994]. Although some studies [e.g., *Zilitinkevich et al.*, 1999] have included nonlocal transport in high-order TKE closure

models, existing observations of the second- and third-order moments seem inadequate for a definitive validation of these more complicated PBL models. Therefore, we suggest further developing the nonlocal PBL schemes such as YSU and ACM2 because of their consistency with the observed fluxes and coherent structure of the convective PBL. This requires further studying the correlation of the eddy diffusivity and the vertical velocity variance $\overline{w'^2}$ [*Hunt et al*., 1988a], the shape and magnitude of the nonlocal fluxes for heat, moisture, and momentum (B. Xie et al., Nonlocal momentum mixing in the planetary boundary layer, manuscript in preparation, 2013), and the entrainment physics with varying heating and shear [*Sullivan et al*., 1998], by LES data sets and field experiments. The current PBL schemes in the WRF model are developed for clear skies, the cloud induced eddies can be considered to be parameterized. In light of the simulated PBL structure's strong dependence on sky conditions and solar radiation, accuracy in cloud cover predictions is important. Possible physical parameterizations that should be considered for improvements to cloud predictions include microphysics, cumulus, and radiation processes.

[59] **Acknowledgments.** This work was supported by grants SRFI11IPO01 and ECWW09EG04 and the Fok Ying Tung Graduate School (NRC06/07.SC01). The first author appreciates the Overseas Research Award from the Hong Kong University of Science and Technology that supported his exchange study in the UK. J. C. R. Hunt acknowledges funding from the Mechanical Engineering Department of the University of Hong Kong and from the Malaysian Commonwealth Studies Centre of Cambridge University.

## References

Baklanov, A., et al. (2007), Integrated systems for forecasting urban meteorology, air pollution and population exposure, *Atmos. Chem. Phys.*, *7*, 855–874.

Barlow, J. F., A. Dobre, R. J. Smalley, S. J. Arnold, A. S. Tomlin, and S. E. Belcher (2009), Referencing of street-level flows: Results from the DAPPLE 2004 campaign in London, UK, *Atmos. Environ.*, *43*, 5,536–5,544.

Barlow, J. F., T. M. Dunbar, E. G. Nemitz, C. R. Wood, M. W. Gallagher, F. Davies, E. O'Connor, and R. M. Harrison (2011), Boundary layer dynamics over London, UK, as observed using Doppler lidar during REPARTEE-II, *Atmos. Chem. Phys.*, *11*(5), 2,111–2,125, doi:10.5194/acp-11-2111-2011.

Bohnenstengel, S. I., S. Evans, P. A. Clark, and S. E. Belcher (2011), Simulations of the London urban heat island, *Q. J. R. Meteorol. Soc.*, *137*, 1,625–1,640, doi:10.1002/qj.855.

Carruthers, D. J., R. J. Holroyd, J. C. R. Hunt, and W. S. Weng (1994), UK-ADMS: A new approach to modelling dispersion in the Earth's atmospheric boundary layer, *J. Wind Eng. Ind. Aerodyn.*, *52*, 139–153.

Caughey, S. J., and S. G. Palmer (1979), Some aspects of turbulence structure through the depth of the convective boundary layer, *Q. J. R. Meteorol. Soc.*, *105*, 811–827.

Chan, A., J. C. H. Fung, and A. K. H. Lau (2013), Influence of urban morphometric modification on regional boundary-layer dynamics, *J. Geophys. Res. Atmos.*, *118*, 2,729–2,747, doi:10.1002/jgrd.50263.

Cimorelli, A. J., S. G. Perry, A. Venkatram, J. C. Weill, R. J. Paine, R. B. Wilson, R. F. Lee, W. D. Peters, and R. W. Brode (2005), AERMOD: A dispersion model for industrial source applications. Part I: General model formulation and boundary layer characterization, *J. Appl. Meteorol.*, *44*, 682–693, doi:10.1175/JAM2227.1.

Deardorff, J. W. (1972), Numerical investigation of neutral and unstable planetary boundary layers, *J. Atmos. Sci.*, *29*, 91–115.

Driedonks, A. G. M. (1982), Models and observations of the growth of the atmospheric boundary layer, *Boundary Layer Meteorol.*, *23*, 283–306.

Foreman, R. J., and S. Emeis (2012), A method for increasing the turbulent kinetic energy in the Mellor-Yamada-Janjić boundary-layer parametrization, *Boundary Layer Meteorol.*, *145*, 329–349.

García-Díez, M., J. Fernández, L. Fita, and C. Yagüe (2013), Seasonal dependence of WRF model biases and sensitivity to PBL schemes over Europe, *Q. J. R. Meteorol. Soc.*, *139*, 501–514, doi:10.1002/qj.1976.

Harrison, R. M., et al. (2012), Atmospheric chemistry and physics in the atmosphere of a developed megacity (London): An overview of the REPARTEE experiment and its conclusions, *Atmos. Chem. Phys.*, *12*, 3,065–3,114.

Holtslag, A. A. M., and B. A. Boville (1993), Local versus nonlocal boundary layer diffusion in a global climate model, *J. Clim.*, *6*, 1,825–1,842, doi:10.1175/1520-0442(1993)006 <1825:LVNBLD>2.0.CO;2.

Hong, S. Y. (2010), A new stable boundary-layer mixing scheme and its impact on the simulated East Asian summer monsoon, *Q. J. R. Meteorol. Soc.*, *136*, 1,481–1,496, doi:10.1002/qj.665.

Hong, S. Y., and H. L. Pan (1996), Nonlocal boundary layer vertical diffusion in a medium-range forecast model, *Mon. Weather Rev.*, *124*, 2,322–2,339, doi:10.1175/1520-0493(1996)124 <2322:NBLVDI>2.0.CO;2.

Hong, S. Y., Y. Noh, and J. Dudhia (2006), A new vertical diffusion package with an explicit treatment of entrainment processes, *Mon. Weather Rev.*, *134*, 2,318–2,341, doi:10.1175/MWR3199.1.

Hunt, J. C. R., J. C. Kaimal, and J. E. Gaynor (1988a), Eddy structure in the convective boundary layer—New measurements and new concepts, *Q. J. R. Meteorol. Soc.*, *114*, 827–858.

Hunt, J. C. R., R. H. Holroyd, and D. J. Carruthers (1988b), Preparatory studies for a complex dispersion model, CERC Report HB9/88.

Hunt, J. C. R., S. Bohnenstengel, S. E. Belcher, and Y. Timoshkina (2012), Implications of climate change for expanding cities world-wide, Proc. Inst. Civil Engineers – Urban Design and Planning.

Janjić, Z. I. (1990), The step-mountain coordinate: Physical package, *Mon. Weather Rev.*, *118*, 1,429–1,443, doi:10.1175/1520-0493(1990)118<1429: TSMCPP>2.0.CO;2.

Janjić, Z. I. (2002), *Nonsingular Implementation of the Mellor-Yamada Level 2.5 Scheme in the NCEP Meso Model, NCEP Off. Note 437*, NCEP, Camp Springs, MD, pp. 61.

Kwok, R., J. C. H. Fung, A. K. H. Lau, and Z. S. Wang (2012), Tracking emission sources of sulfur and elemental carbon in Hong Kong/Pearl River Delta region, *J. Atmos. Chem.*, *69*, 1–22.

Lenschow, D. H., J. C. Wyngaard, and W. T. Pennell (1980), Mean-field and second-moment budgets in a baroclinic, convective boundary layer, *J. Atmos. Sci.*, *37*, 1,313–1,326.

Mellor, G. L., and T. Yamada (1982), Development of a turbulence closure model for geophysical fluid problems, *Rev. Geophys.*, *20*, 851–875, doi:10.1029/RG020i004p00851.

Moeng, C.-H., and P. P. Sullivan (1994), A comparison of shear- and buoyancy-driven planetary boundary layer flows, *J. Atmos. Sci.*, *51*, 999–1,022.

Moeng, C.-H., and J. C. Wyngaard (1986), An analysis of closures for pressure-scalar covariances in the convective boundary layer, *J. Atmos. Sci.*, *43*, 2,499–2,513.

Moeng, C.-H., and J. C. Wyngaard (1989), Evaluation of turbulent transport and dissipation closures in second-order modeling, *J. Atmos. Sci.*, *46*, 2,311–2,330.

Nakanishi, M., and H. Niino (2009), Development of an improved turbulence closure model for the atmospheric boundary layer, *J. Meteorol. Soc. Jpn.*, *87*, 895–912.

Ng, E., C. Yuan, L. Chen, C. Ren, and J. C. H. Fung (2011), Improving the wind environment in high-density cities by understanding urban morphology and surface roughness: A study in Hong Kong, *Landscape Urban Plann.*, *101*(1), 59–74, doi:10.1016/j.landurbplan.2011.01.004.

Nieuwstadt, F. T. M. (1981), The steady-state height and resistance laws of the nocturnal boundary layer: Theory compared with Cabauw observations, *Boundary Layer Meteorol.*, *20*, 3–17.

Nieuwstadt, F. T. M., and J. C. R. Hunt (2003), Boundary layers: Coherent structures, *Encyclopedia of Atmospheric Sciences*, pp. 228–234, Elsevier Science Ltd, London, U.K.

Pleim, J. E. (2007a), A combined local and nonlocal closure model for the atmospheric boundary layer. Part I: Model description and testing, *J. Appl. Meteorol. Climatol.*, *46*, 1,383–1,395, doi:10.1175/JAM2539.1.

Pleim, J. E. (2007b), A combined local and nonlocal closure model for the atmospheric boundary layer. Part II: Application and evaluation in a mesoscale meteorological model, *J. Appl. Meteorol. Climatol.*, *46*, 1,396–1,409, doi:10.1175/JAM2534.1.

Pleim, J. E., and J. S. Chang (1992), A non-local closure model for vertical mixing in the convective boundary layer, *Atmos. Environ. Part A*, *26*, 965–981.

Shin, H. H., and S. Y. Hong (2011), Intercomparison of planetary boundary-layer parameterizations in the WRF model for a single day from CASES-99, *Boundary Layer Meteorol.*, *139*, 261–281, doi:10.1007/s10546-010-9583-z.

Skamarock, W. C., J. B. Klemp, J. Dudhia, D. O. Gill, D. M. Barker, M. G. Duda, X.-Y. Huang, W. Wang, and J. G. Powers (2008), A description of the advanced research WRF version 3, in *NCAR Tech. Note TN-475 +STR*, NCAR, Boulder, CO, pp. 113.

Stull, R. B. (1984), Transilient turbulence theory. Part I: The concept of eddy-mixing across finite distances, *J. Atmos. Sci.*, *41*, 3,351–3,367, doi:10.1175/1520-0469(1984)041<3351:TTTPIT>2.0.CO;2.

Sullivan, P. P., C.-H. Moeng, B. Stevens, D. H. Lenschow, and S. D. Mayor (1998), Structure of the entrainment zone capping the convective atmospheric boundary layer, *J. Atmos. Sci.*, *55*, 3,042–3,064.

Troen, I., and L. Mahrt (1986), A simple model of the atmospheric boundary layer: Sensitivity to surface evaporation, *Boundary Layer Meteorol.*, *37*, 129–148, doi:10.1007/BF00122760.

Willmott, C. J. (1981), On the validation of models, *Phys. Geogr.*, *2*, 184–194.

Wyngaard, J. C., and R. A. Brost (1984), Top-down and bottom-up diffusion of a scalar in the convective boundary layer, *J. Atmos. Sci.*, *41*, 102–12.

Xie, B., J. C. H. Fung, A. Chan, and A. Lau (2012), Evaluation of nonlocal and local planetary boundary layer schemes in the WRF model, *J. Geophys. Res.*, *117*, D12103, doi:10.1029/2011JD017080.

Zhang, R., G. Sarwar, J. C. H. Fung, A. K. H. Lau, and Y. Zhang (2012), Examining the impact of nitrous acid chemistry on ozone and PM over the Pearl River Delta Region, *Adv Meteorol.*, doi:10.1155/2012/140932.

Zilitinkevich, S. S., V. M. Gryanik, V. N. Lykossov, and D. V. Mironov (1999), Third-order transport and non-local turbulence closures for convective boundary layers, *J. Atmos. Sci.*, *56*, 3,463–3,477.